Comparison of Two X-ray Detection Systems Used to Investigate Properties of Normal and Malignant Breast Tissues.

COMPARISON OF TWO X-RAY DETECTION SYSTEMS USED TO INVESTIGATE PROPERTIES OF NORMAL AND MALIGNANT BREAST TISSUES.

BY

DUAA F. ALAROUI, B.Sc.

A THESIS

SUBMITTED TO THE DEPARTMENT OF RADIATION SCIENCES

AND THE SCHOOL OF GRADUATE STUDIES

OF MCMASTER UNIVERSITY

IN PARTIAL FULFILMENT OF THE REQUIREMENTS

FOR THE DEGREE OF

MASTER OF SCIENCE

Master of Science (2018)   McMaster University

(Radiation Sciences Graduate Program)   Hamilton, Ontario, Canada

TITLE: Comparison of Two X-ray Detection Systems Used to
                          Investigate Properties of Normal and Malignant Breast
                          Tissues.

AUTHOR: Duaa F. Alaroui

                          B.Sc., (Applied Physics)

                          Taibah University, Madinah, Saudi Arabia

SUPERVISOR: Dr. Michael Farquharson

NUMBER OF PAGES: xiv, 94

To the most wonderful, generous and supportive mom and dad ever. I dedicate this work to you.

Abstract

The present study was implemented using two different X-ray detection systems; a monochromatic X-ray system for X-ray Fluorescence (XRF) and Angular Dispersive X-ray Diffraction (ADXRD) techniques, and a combined Polarized Energy Dispersive X-ray Fluorescence (PEDXRF) and Energy Dispersive X-ray Diffraction (EDXRD) system. As both of these systems involve different techniques, the primary objective of this study was to evaluate the performance and accuracy of each system using results achieved from XRF measurements. The assessment of the two systems was carried out by investigating invasive ductal carcinoma (IDC) of breast and normal surrounding breast tissues. The results established from the two XRF systems are in a very good agreement with each other. The statistical analysis reveals a significant and measurable increase at $P < 0.01$ in the concentration of K, Ca, Zn, Rb and Fe ($P < 0.05$) in the tumor tissue when compared with the healthy tissue. However, the levels of Cl, Cu and Br attained by both systems have not demonstrated a statistically significant difference between the normal and cancerous tissues. Investigating the structural components of the same breast tissues using of the X-ray Diffraction (XRD) spectrometers incorporated in both systems indicated a statistically significant difference in the components of normal and malignant samples. Furthermore, the results have shown a remarkable increase in the fibrous and water contents of

the tumour tissue at $P < 0.01$, and a significant increase in the adipose content of the normal tissue at $P < 0.01$. The results acquired from both XRD approaches were shown to be statistically compatible with each other. Overall, the comparisons between the two X-ray detection systems have shown tremendous results for the combined PEDXRF and EDXRD system for the purpose of classifying normal and tumor breast tissues.

Acknowledgements

I would first like to greatly thank my supervisor Dr. Michael Farquharson for his endless guidance, support and positive encouragement. I have gained a great amount of experience and valuable knowledge throughout working with you. Thank you for giving me the opportunity to work with you and in collaboration with great research group members. I would also like to thank my committee members, Dr. David Chettle and Dr. Thomas Farrell for kindly taking the time to participate in my thesis committee. I have acquired extensive knowledge from your valuable input, insightful comments and suggestions. My sincere gratitude to Dr. Soo Hyun Byun for his continuous support, motivation and joyfulness. Thank you for spreading smiles and happiness among our department.

I would also like to especially and exceedingly thank my peers Eric Johnston, Matthew Bernacci and Xin Tong. Thank you, when I know thank you isn't enough, for being awesome people. It has been a great pleasure to work alongside the most kind, funny and talented people. Your immense knowledge, unwavering support and great personalities will remain forever in my memory. Special thanks also goes to my wonderful officemates at 104B: Devin Burke, Michelle Lord (My DiaBudy), Tomas Urlich, Jessie Ma, and Xin Tong, for making the past two years very special. Yum-Yum Fridays, Starbucks trips, Birthday surprises and so many other unforgettable

memories will be treasured forever.

A very special thank you goes to my everlasting cheerleaders Eamy and Zainab, the best friends I could ever ask for! Thank you for being there 24/7 for me and for providing me with every possible kind of love and support since the day we met. You both will forever hold the greatest place in my heart.

With a huge sized green heart, I would like to express my gratitude and appreciation to the Government of Saudi Arabia for their unlimited amount of support, assistance and encouragement during the past two years. Your continual support has made this study achievable.

Last but definitely not least, I would like to thank my wonderful parents and siblings for their incredible support and endless love. At every step of the way, your love did not leave me for a moment. There is no words could ever describe how much I love you. This is all for you.

Notation and abbreviations

ADXRD Angular Dispersive X-Ray Diffraction

EDXRD EDXRD Energy Dispersive X-Ray Diffraction

EDXRF EDXRF Energy Dispersive X-Ray Fluorescence

HPGe High-Purity Germanium

MCA Multiple Correspondance Analysis

MDL Minimum Detection Limit

NAA Neutron Activation Analysis

INAA Instrumental Neutron Activation Analysis

PCA Principal Component Analysis

PEDXRF Polarized Energy Dispersive

PIXE Particle-Induced Xray Emission

PLA Polylactic Acid

SSD Silicon Drift Detector

SNR Signal-to-Noise Ratio

TXRF Total Reflection X-Ray Fluorescence

XRD X-Ray Diffraction

XRF X-Ray Fluorescence

Contents

List of Figures

List of Tables

Chapter 1

Introduction

1.1   Literature Review

Breast cancer is the most common cancer in women and ranks as second in the world in terms of cancer deaths (Parkin *et al.*, 2001). Over the years, efforts have been devoted to developing techniques that can investigate the role of trace elements in biological systems and their structural composition in order to understand their correlation to morbid conditions. The initial screening procedures include x-ray mammography and ultrasound, sometimes followed by palpation (Volynskaya *et al.*, 2008). Examining breast tissues is heavily dependent on the breast density (Scott *et al.*, 2017) and this variation in density leads to a reduction in accuracy for the aforementioned procedures. Tissue biopsy therefore remains the most standard practise in the diagnosis of the carcinogenesis (Tadrous *et al.*, 2003). However, several analytical techniques that help differentiate normal and cancerous tissue have also been in development over the past few decades. Some of these techniques are based on the assumption that the concentration of essential elements varies between cancerous and normal tissue.

Essential elements are involved in various metabolic and biological processes and play a vital role as tumour biomarkers and prognostic factors in breast cancer (Silva *et al.*, 2012a). The International Agency for Research on Cancer has categorized trace elements and their role in tumorigenesis (Costello and Franklin, 1998; McLaughlin and Schuman, 1983). The role of trace elements in the processes leading to cancer has been interrogated in a number of studies (Schrauzer, 1980; Rizk and Sky-Peck, 1984; Geraki and Farquharson, 2001; Silvera and Rohan, 2007). Elevated trace element concentrations were observed in malignant breast tissues (Ng *et al.*, 1997; Cui *et al.*, 2007; Farquharson *et al.*, 2008). A recent study has outlined the association between the existence of some trace elements and their role in developing breast cancer, in addition to addressing recent insights on the molecular mechanisms involved by metals in carcinogenesis (Lappano *et al.*, 2017). The study demonstrated that the exposure to metals such as Zn, Cd and Ni may lead to increase breast cancer risk, as elevated levels of these elements have been measured in breast tumor specimens.

Non-destructive techniques involving radiation have gained ground as a powerful diagnostic tool over the last couple of decades. Trace element analysis using non-destructive techniques such as X-ray fluorescence (XRF) and Neutron Activation Analysis (NAA) have shed light on the discernible features of normal and malignant tissues in the human body. The key principle on which these techniques are based is the interaction of radiation with matter. The present study focuses on utlizing XRF techniques to differentiate between normal and tumor breast tissues. Several studies were carried out in this regard using different XRF methods and are summarized as follows.

Energy dispersive x-ray fluorescence (EDXRF) is a popular technique widely employed in trace element studies and characterized by simultaneously identifying trace elemental compositions within a wide range of concentrations in addition to its simple operation and affordable components (Abuhani *et al.*, 2014). Rizk and Sky-Peck analyzed breast tissues obtained from patients with primary carcinoma by means of EDXRF and observed elevated levels of trace elements in the affected tissues (Rizk and Sky-Peck, 1984). Using the same technique, Silva *et al.* (2013) investigated the elements Ca, Cu, Fe and Zn in neoplastic and normal breast tissue and correlated these with the spatial distributions of the trace elements obtained by a μ-XRF system. The results revealed that a relation exists between the expression of the trace elements Fe, Cu and vascular endothelial growth factor. Another application of this technique was performed recently to observe the elemental composition of breast calcifications (Scott *et al.*, 2017) using Energy-dispersive X-ray spectroscopy in a scanning electron microscope (SEM-EDS) to examine the elemental composition of calcifications contained within histological sections of breast tissue biopsies. The study assessed the ratios of Ca:P, Mg:Ca and Na:Ca between benign and malignant from 66 calcifications in 31 specimens. A significant difference in Na:Ca was discovered, which has potential for revealing malignant changes in the vicinity of a core needle biopsy. Geraki *et al.* (2003) employed synchrotron based XRF to quantify the concentrations of the trace elements Fe, Cu and Zn in breast tissues. Trace element levels in invasive ductal carcinoma of the breast when compared to normal tissue, were found to have significantly increased levels of these elements. Cui *et al.* (2007) measured tissue concentrations of elements Zn, Se, Ca and Fe using X-ray fluorescence on the beamline of the Advanced Photon Source at the Argonne National Laboratory. 14.1-keV X-rays were

used to illuminate a 0.5-mm-diameter area on each mounted sample collected from a total of 252 matched case-control pairs. The study suggested a possible increase in risk of subsequent breast cancer among women with benign breast disease due to the increased levels of Zn, Fe, and Ca. Breast sample measurements were carried out using a synchrotron X-ray Fluorescence Microprobe, a powerful tool for simultaneous trace element analysis. It was inferred that the concentrations of elements Ca, Fe, Cu and Zn were higher in the areas of malignancy (Al-Ebraheem *et al.*, 2009). Similar studies were carried out using μ-XRF to obtain two-dimensional distribution of trace elements Ca, Fe, Cu and Zn in normal and malignant breast tissue samples (Silva *et al.*, 2012b). Qualitative and quantitative results showed that the pairs of elements Ca-Zn and Fe-Cu correlated in malignant breast tissues.

The elemental analysis of benign and malignant neoplastic tissues has been performed on the basis of Total Reflection X-ray Fluorescence (TXRF) spectroscopy. The limitation on the detection limit due to the background noise can be overcome to some extent by employing TXRF (Majewska *et al.*, 2007). Analogous to TXRF spectroscopy, polarizing beam EDXRF (PEDXRF) is capable of minimizing the background arising from Compton scattering and so improve signal to noise ration (SNR), and hence can significantly improve minimum detection limits (MDLs) in a similar order as TXRF. The reduction of scatter can be achieved by utilizing a powerful x-ray tube and placing equipment in a Cartesian or tri-axial geometry (Heckel *et al.*, 1992; Abuhani *et al.*, 2014). PEDXRF has been effectively employed in numerous applications (Heckel *et al.*, 1991, 1992; Marguí *et al.*, 2006; Zhan, 2005; Abuhani *et al.*, 2014). Particle-Induced X-Ray Emission (PIXE) was used to study the variations in trace

elemental concentrations between normal and malignant human breast tissue specimens by Raju *et al.* (2006). Trace elements (Ca, Fe, Cu and Zn) studies in breast cancer tissues using Laser ablation inductively coupled plasma mass spectrometry (LA-ICP-MS) was carried out to investigate their distribution and its possible application for tumor diagnostic and prognostic purposes. The levels of these elements were found to be high in cancerous tissues compared to benign ones (de Vega *et al.*, 2017). Instrumental Neutron activation analysis (INAA) was employed to determine elements in cancerous and normal breast tissue. Five minor elements (Cl, K, Na, Mg, P) and 15 trace elements (As, Br, Co, Cr, Cs, Cu, Fe, Hg, Mn, Rb, Sb, Se, Sc, Sr, and Zn) in cancerous and normal breast tissue from 30 patients of four clinical stages were analysed and the results showed an increase in the concentrations of several elements in the cancerous breast tissue (Garg *et al.*, 1994). Similar studies employing INAA were also carried out on 46 paired samples of excised cancerous tissues (Ng *et al.*, 1997). Apart from fluorescence studies, diffraction studies are also prominent in the quantification of trace elements and evaluation of molecular structures in biological tissues.

Incoherent and coherent scattering have been shown to be better at determining important quantities related to skeletal status. A number of studies utilized Compton scattering as a powerful tool to differentiate between examined biological specimens and to determine electron density of different tissues. Al-Bahri and Spyrou (1998), developed a system utilizing Compton scatter with an Am-241 source. This was in fact the first study to use Compton scattering in characterizing breast tissue. The results showed that adipose had lower electron density than the malignant tumour samples. The discrepancies in the results were verified by Ryan *et al.* (2005) who

performed a more extensive study, with a larger range of tissues, and found comparable differences. One study suggested the use of scatter to create diffraction data has potential in the detection of breast cancer (Speller, 1999). The process of X-ray diffraction (XRD) is based on Bragg's law shown in the following equation, and it is typically employed in crystalline structure studies to determine the inter-atomic and inter-molecular distances.

$$n\lambda = 2dsin\frac{\theta}{2} \tag{1.1}$$

Where,

λ is the X-ray wavelength

d is the inter-planar spacing

θ is the total angle through which the incident X-rays are scattered

The scattering amplitude of coherent scattering is the Fourier transform of the electron density of the object. Though the observable quantity is the intensity, the scattering pattern yields a detailed image of the structure of the object on the atomic and molecular level. Biological tissues; though characterized by short-range order, still give rise to diffraction patterns. In such cases, the patterns are expressed in terms of momentum transfer, which is a combination of beam angle and energy can be used to investigate different distances between the planes.

XRD experiments can be carried out in two different modes; angular and energy dispersive. In angular dispersive X-ray diffraction (ADXRD), the X-ray energy is fixed (monochromatic) and the scatter intensity is measured as a function of the incident X-ray angle made with the detector. On the other hand, in energy dispersive X-ray

diffraction (EDXRD), the scatter intensity is measured across a range of energies using a polychromatic X-ray source while keeping the scattering angle fixed. Each modality has its own advantages and limitations. A high angular resolution can be achieved from ADXRD whereas the energy resolution of EDXRD set up relies on the size and shape of the scattering volume, which decreases as the primary beam passes through the detector collimator (Moss *et al.*, 2017). ADXRD requires moving the detector or x-ray source during the data collection whereas EDXRD can be performed with static equipment. Due to the narrow collimation required when performing EDXRD experiments, with the purpose of accurately determining θ, the output beam flux is greatly reduced, and hence long measuring times are needed (OFlynn *et al.*, 2013). Studies on tissue diffraction data (Harding *et al.*, 1987; Kosanetzky *et al.*, 1987) proposed that XRD systems could offer better tissue characterization than conventional transmission CT. Later, several researchers have shown the feasibility of breast tissue characterization by using X-ray diffraction experiments. Evans *et al.* (1991) conducted a preliminary study on the use of forward scatter radiation to characterize breast tissue. They observed prominent features in the diffraction data. Shapes of the distributions differed largely between adipose and fibroglandular tissues whereas only small differences were found between carcinomas and fibroglandular tissues. Synchrotron X-ray diffraction was used by Scott *et al.* (2016) to determine how the phase composition and crystallographic parameters within calcifications differ with pathology. This study was the first to determine crystallite size and lattice parameters in breast calcifications. It was found that the crystallite size and lattice parameters in breast calcifications resemble the changes in these parameters with age observed in fetal bone. This study has also suggested that these calcifications contain

a small proportion of magnesium whitlockite, and that this proportion increases from benign, to *in situ*, to invasive cancer.

Wide angle studies by LeClair *et al.* (2006) measured the diffraction patterns of three types of breast tissue: normal fibroglandular tissue, adipose and infiltrating duct carcinoma. Narten and Levy developed a semi-analytical model to extract differential linear scattering coefficients from raw data (Narten and Levy, 1971). Elshemey *et al.* (1999) studied the characteristics of low-angle x-ray scattering in some biological samples by means of a Monte Carlo simulation that includes molecular form factor data. Energies up to 13 keV and sample thickness of 0.3 cm were found to be optimum to observe maximum differences between malignant and benign samples. Small angle scattering typically refers to investigations at momentum transfer values of less than 0.25 nm^{-1}. Small angle studies were successful in showing acceptable or convincing differences between healthy and malignant tissues. The procedure can look at structures of the order of 10 to 1000 nm (Lewis *et al.*, 2000). X-ray diffraction data obtained at photon energies of 17.44 keV (Kα radiation of Mo) and 6.93 keV (Kα radiation of Co) from healthy (adipose and glandular) and cancerous human breast tissue suggested that strong differences between actual and equivalent breast tissue materials occur at low and medium scattering angles (Poletti *et al.*, 2002). Round *et al.* (2005) found a statistically significant difference between normal tissue and tumor using small angle studie employing a laboratory X-ray source.

A 2007 study employed a diffraction microCT system at a synchrotron radiation source and obtained images of small breast tissue samples highlighting the fatty regions within the samples. The study concluded that diffraction techniques can be used to obtain better contrast between tissue types. Also, the study ruled out the

significance of attenuation correction in case of small tissue samples at mammographic energies (Griffiths *et al.*, 2007). The efficacy of angular dispersive X-ray diffraction data processed using multivariate analysis in classifying secondary colorectal liver cancer tissue and normal liver tissue was tested and it was found that ADXRD data are statistically different between the tissues and confirmed that the x-ray diffraction data analyzed using multivariate analysis have the potential to be used as a method of tissue classification (Theodorakou and Farquharson, 2009). Similar studies carried out using the scattering profiles of 106 healthy and pathological human breast samples also proved that the technique allows to classify 91.5% of the samples correctly (Conceição *et al.*, 2010).

Similar to ADXRD, EDXRD is also a promising technique for breast tissue characterization. Scattering properties of excised breast tissues were measured using an energy dispersive x-ray diffraction system over the momentum transfer range of 0.70 to 3.50 nm^{-1} and the results were compared with the histological analysis for each individual sample. This study established the possibility of characterizing the breast tissue based on the shapes of the scatter spectrum and on its relative intensity. Momentum transfers in the range of 1.0 to 1.8 nm^{-1} were found to be promising for better demarcation of the scatter signal (Kidane *et al.*, 1999). An optimized system called multifocal XRD that combines EDXRD information at different scattering angles, was developed by Marticke *et al.* (2017) who utilized it as a second control level when conventional mammography results were unclear because of overly high breast density. In order to assess the separation power of the method and to determine the radiation dose required to obtain nearly ideal separation, breast phantoms with and

without cancerous nodules were simulated. The results have revealed that both sensitivity and specificity of the method were acceptable even when the delivered dose was not high. Also, the variation in breast densities does not influence the detectability of the tumor or the order of magnitude of the required dose. EDXRD data collected for breast tissue samples were combined with Monte Carlo simulations to correct for compositions and differentiate between adipose and fibrous tissue (Geraki *et al.*, 2003). LeClair *et al.* (2006) described a semi-analytic model that can be applied to energy dispersive x-ray diffraction data and suggested that the combination forms an excellent approach to identify and classify unknown samples. Imaging techniques combined with diffraction studies were found to reduce sample categorization errors (Griffiths *et al.*, 2008). EDXRD systems developed were being optimized from time to time for better clinical applications (Chaparian *et al.*, 2010). Optimum parameters for obtaining high quality diffraction patterns of breast tissue were determined. Latest developments in the field include optimization of mono- and multifocal collimation systems for EDXRD-based virtual biopsy in mammography (Marticke *et al.*, 2015) and EDXRD system coupled with low divergence capillary optics (Sosa *et al.*, 2017). In a recent study, a pixellated, energy-resolving X-ray detector that can provide ADXRD and EDXRD data has been developed. The chief feature of this set up is that it can utilize the benefits of both the modalities (O'Flynn *et al.*, 2013).

1.2   Project Objectives

The present study was performed on breast tissues obtained from breast cancer patients and aimed at achieving two objectives. The first was to compare the performance between two different XRF spectrometers; the Huber XRF spectrometer and Polarized Energy Dispersive XRF spectrometer (PEDXRF). Both of these systems are capable of measuring trace transition metals in biological samples, however, they have distinguishable differences including, but not limited to, measurement acquisition time and scatter rejection. This study concentrated on exploring these features by utilizing the two previously mentioned spectrometers to analyze the following trace elements: Cl, K, Ca, Fe, Cu, Zn, Br, and Rb in 19 matched pairs of breast tissue specimens. The second goal of the study was to investigate the structural components (i.e. Adipose, fibrous and water) of the same breast tissues that were examined for an XRF comparison study. Exploring the molecular structure of biological samples can be accomplished by employing X-ray diffraction spectroscopy as it can provide precise information on the investigated material. The two approaches of XRD spectroscopy (EDXRD and ADXRD), were used to carry out the XRD experiment. As such this second study compared the results of these two modalities.

All the aforementioned techniques, when combined together, become more promising as they provide more accurate information on tissues elemental composition and structural components. Achieving these objectives will greatly help not only us, but also the breast cancer research community in understanding the mechanism behind this disease and the way it develops, which can be essential to aid in diagnosis or treatment.

Chapter 2

Background and Fundamentals

X-rays are a form of ionizing electromagnetic radiation that interacts with matter and has a wavelength that falls in the Angstrom (10^{-11} m) region (Als-Nielsen J., 2001). In this region, there are primarily three types of x-ray interactions with a material to consider. The incident beam can be completely absorbed by the target atom via a process called photoelectric absorption, it can deflect from its initial direction through an angle θ, and this interaction can be defined as Compton scattering, or it can also interact coherently with the atom throughout a process called Rayleigh scattering. Chapter Two will explain in further detail the physical processes behind the previously mentioned interactions, in addition to the theory of generating an x-ray beam as it plays a pivotal role in obtaining data. The last section of this chapter will shed light on the theoretical framework of the employed XRF and XRD spectrometers; this involves their modalities, concepts and geometrical setup. More details about the methodology of this study will be presented in chapter 3.

2.1   Interactions of X-rays with Matter

2.1.1   Photoelectric Absorption

The photoelectric effect results from the interaction of an incident X-ray beam with an electron in the material of interest. Throughout this process, the incident photon is fully absorbed and the electron is ejected from its shell with a kinetic energy of (E_e). This can happen only if the incident photon has a higher or equal energy (hv) to the energy binding the electron to the atom (E_b). The kinetic energy of the electron is provided by equation 2.1 (Knoll, 2000).

$$E_e = (hv) - E_b \qquad (2.1)$$

In the case of atoms with low atomic numbers, most photoelectric interactions occur with the K-shell electrons; as the electrons in this shell are tightly bound to the nucleus. In contrast, for the atoms with high atomic numbers, the binding energy is much higher, and therefore, a higher incident energy is required to eject electrons from their innermost shells (K- shells). However, if the incident energy is inadequate to eject an inner shell electrons, the photoelectric processes are most probable to occur at the outermost shells. As a result, it can be concluded that the higher the atomic number and the lower the energy of the incident beam, the more likely the photoelectric effect has to occur (Curry *et al.*, 1990). Figure 2.1 illustrates the photoelectric absorption effect which results in an emitted photoelectron and a released characteristic x-rays. Nevertheless, the electron ejection resulting from the photoelectric absorption will lead to an excited target atom. To de-excite, the vacancy in the shell is promptly filled by another electron from a higher orbital shell, subsequently

releasing energy in the form of a characteristic x-ray (also called fluorescent) or as an Auger electron.
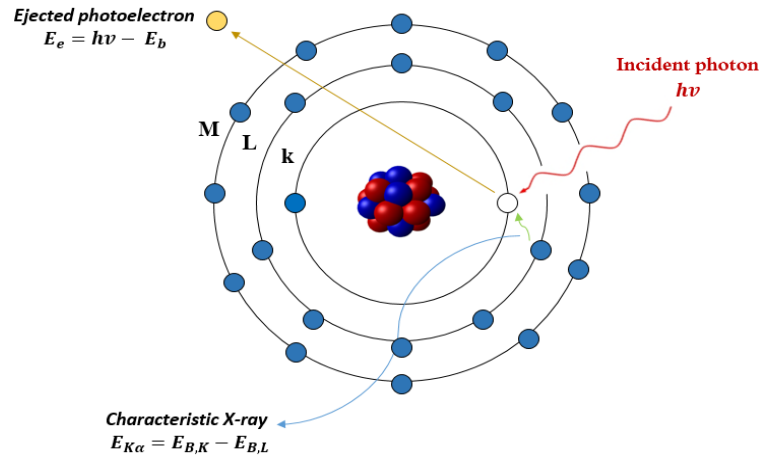
Figure 2.1: Photoelectric effect yielding an ejected photoelectron. A characteristic Kα x-ray results from the transition of an electron from L-shell to fill up the vacancy in K-shell.

The energy of the emitted x-ray photon is given by equation 2.2, and it is equal to the difference between the binding energies of the innermost shell which the electron transfers to, and the outer orbital shell which the electron transfers from.

$$E_{charactrsticx-ray} = (E_b)_{innershell} - (E_b)_{outershell} \tag{2.2}$$

As the electrons are ordered in different orbitals denoted by K, L, M, N, and so on, the emitted characteristic x-rays are labelled according to the orbital shells that are involved in the transition of the electrons. An approprite subscript of α, β, or γ is added next depending on which shell the electron is originated from. In order to differentiate between the subshells involved in the electron transition process, Roman numerals are used. For instance, if the vacancy is created in the K-shell and an

electron falls from L_{III} subshell to fill this vacancy, a Kα characteristic x-ray will be emitted, as shown in Figure 2.1, with energy given by equation 2.3.

$$E_{K\alpha} = (E_b)_{k-shell} - (E_b)_{L-shell} \qquad (2.3)$$

However, since the atom contains a number of shells, the vacancy in the K- shell can also be filled by an electron from M_{III} subshell. This transition results in emitting a Kβ characteristic x-ray with a higher energy demonstrated in equation 2.4. The increase in energy is due to higher atomic shells having higher binding energies, which also increases with increasing atomic number (Knoll, 2000).

$$E_{K\beta} = (E_b)_{K-shell} - (E_b)_{M-shell} \qquad (2.4)$$

The second emission that can take place following the photoelectric absorption process is Auger electron emission. In contrast to the characteristic x-rays emission, the process of filling an inner shell vacancy is associated with ejecting an outer shell electron from the same target atom, defined as an Auger electron. The kinetic energy of an Auger electron can be expressed as the difference between the energy lost by the electron that made the transition, and the binding energy from which the electron was ejected from (Curry et al., 1990). The amount of this energy depends on the atomic number (Z); in which the lower the Z number and binding energies the more likely the Auger electron emission is to occur. The probability of emitting Auger electron competes with the probability of producing characteristic x-rays. This can be quantified by introducing the X-ray fluorescence yield, ω, which is defined as

the fraction of the total number of the emitted characteristic x-rays during the de-excitation process, to the number of the absorbed x-rays (Knoll, 2000). For example, the fluorescent yield of K-shell, ω_k can be calculated as the ratio of the number of all emitted photons by all K spectral lines to the number of K-shell vacancies formed. ω_k is given by equation 2.5, where A is a constant on the order of 10^6 for the K series,

$$\omega_k = \frac{Z^4}{A + Z^4} \tag{2.5}$$

The fluorescent yield depends significantly on the atomic number Z in which the higher the atomic number, the higher the fluorescent yield result. The probability of emitting an Auger electron is 1-ω (Bushberg *et al.*, 2003).

2.1.2 Coherent Scattering

One of the interactions that causes scattered radiation in a material is coherent scattering (also known as Rayleigh, or elastic scattering) and is as the one that leads to the phenomenon of x-ray diffraction (Post, 1999). Figure 2.2 illustrates the process of coherent scattering. In this process, the incident photon interacts coherently with the entire target atom instead of interacting with individual electrons. The incident photon causes the electrons of the atom to oscillate as a result of the electromagnetic field, and emit a scattered photon possessing the same wavelength as the incident photon. The scattered photon can be emitted in any direction except the direction of oscillation. However, this interaction will have no influence on the atom's electronic state as the electrons will return to their original positions following the release of the scattered photon.

The scattered photon will leave the atom in a new direction but maintain its
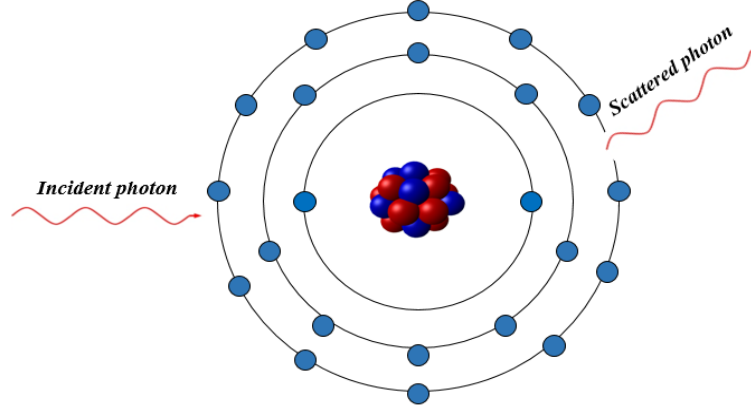
Figure 2.2: Coherent scattering causes the incident photon to interact with an atom, resulting in a scattered photon in a different direction but with the same energy as the incoming photon.

energy, that of the incident photon (Knoll, 2000; Post, 1999). In the case of unpolarized radiation, and the energy of the incident photon below a few hundred keV, i.e. less than the rest mass energy of electron ($m_o c^2$) scattering off a target atom, the differential cross section for coherent scattering is valid and given by equation 2.6 (Theodorakou and Farquharson, 2008)

$$\frac{d_e \sigma_{coh}}{d\Omega} = \frac{d_e \sigma_o}{d\Omega} F^2(x) = \frac{r_0^2}{2}(1 + cos^2\theta)F^2(x) \tag{2.6}$$

Where, $\frac{d_e \sigma_o}{d\Omega}$ is the classical or Thomson cross section, r_o is the classical radius of the electron and determined as $\frac{e^2}{m_e c^2}$, the factor $\frac{1+cos^2\theta}{2}$ is obtained from averaging over all incident possible polarization, and $F(x)$ specifies the coherent scatter form factor and corresponds to the following equation (Als-Nielsen J., 2001):

$$F(x) = < 0|\Sigma_{j=1}^z e^{ix.r_j}|0 > \tag{2.7}$$

Where: $x = k - k'$, and it indicates the momentum transferred to the photon

$|0>$ is the ground state function of the atom.

The limiting values of the form scatter at $(x = 0)$ is the atomic number (Z) and at $(x \to \infty)$ the form factors is zero, $F(x \to \infty) = 0$.

Coherent scattering differential cross section differs with the inverse of the atomic number of the atom and photon energy as Z^2 and as E^{-2} respectively, while the probability of coherent scattering to occur increases as the atomic number increases and incident energy decreases (Als-Nielsen J., 2001).

2.1.3   Compton Scattering

The second scattering process of radiation in a material is Compton scattering, also known as inelastic scattering as the incedint photon losses energy after collision with atom. The Compton effect results from the interaction between an incident x-ray photon and an orbital electron as shown in Figure 2.3. The photon to deflect from its initial path through an angle θ. In addition, the electron will gain partial energy from the photon and become ejected from its orbital position as a recoil electron with an energy $E_e = E_\gamma - E'_\gamma$.

The remaining energy of the incident photon will be re-emitted as a secondary x-ray photon with a lower energy. The energy of the scattered photon is given by equation 2.8 (Bushberg *et al.*, 2003).

$$E'_\gamma = \frac{E_\gamma}{1 + \frac{hv}{m_o c^2}(1 - cos\theta)} \tag{2.8}$$
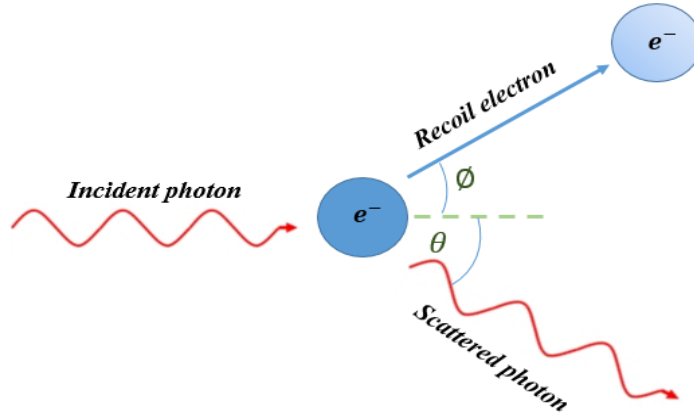
Figure 2.3: Compton scattering occurs from the interaction between the incident photon and an outer shell electron, resulting in a scattered photon in a different path and a recoil electron.

Where $(m_o c^2)$ is the rest mass energy of the electron (511 keV), and the angle θ is the scattering angle of the photon in which the change in energy depends. The probability of Compton scattering depends on the number of available electrons. Therefore, the probability of Compton scattering to take place increases linearly with the increase in atomic number Z (Knoll, 2000). The angle in Compton scattering also plays a critical role, in which the increase in the scatter photon wavelength ($\Delta\lambda$) is heavily dependent on the angle between the scattered photon and recoil electron (Curry et $al.$, 1990).

$$\Delta\lambda = \frac{h}{m_o c}(1 - cos2\theta) \qquad (2.9)$$

The differential cross section for Compton (incoherent) scattering was first determined by Klein and Nishina (KN) and it takes the form shown in equation 2.10 for

unpolarized x-rays beam and a single free electron (Als-Nielsen J., 2001),

$$\left(\frac{d^2\sigma}{d\Omega}\right)_{KN} = \frac{r_e^2}{2}\left(\frac{E'_\gamma}{E_\gamma}\right)^2\left(\frac{E'_\gamma}{E_\gamma} + \frac{E_\gamma}{E'_\gamma} - sin^2\theta\right) \tag{2.10}$$

This form of scattering is more probable to occur at high incident energies, yet, it bears a close similarity to the shape of coherent scattering case.

However, in the case of the bound electron, a correction form factor term, $S(q, Z)$, is included to adjust for the influence of the charge distribution of the other electrons in the target atom, which are by approximation not disturbed by the interaction. Hence, the differential cross section per electron for Compton scattering is given by equation 2.11 (Theodorakou and Farquharson, 2008)

$$\frac{d\sigma_{comp}}{d\Omega} = \frac{d\sigma_{KN}}{d\Omega}S(q, Z) \tag{2.11}$$

For a given absorbing material Compton scattering depends on the electron density which has a vital role in providing a detailed image for the examining biological specimen (Ryan *et al.*, 2005). Nevertheless, at low incident energies, the impact of the electron binding energy leads to an decreases in the cross section. Whereas at higher incident energies, the electron is essentially free, and the cross section declines with increasing photon energy (Als-Nielsen J., 2001).

2.2   X-ray Attenuation

While a monochromatic x-ray beam traverses throughout a target material, its intensity declines by either the absorption or scattering of photons from the beam.

Attenuation occurs once a photon has undergone any interaction (i.e. photoelectric absorption, Compton or coherent scattering). The attenuated x-ray photons can be distinguished by a fixed probability of interaction per unit path length in the target material (Knoll, 2000). The attenuation coefficient, of removing an x-ray photon from the beam for multiple interactions is as the total of all the attenuation coefficients corresponding to each interaction as follows:

$$\mu_{sum} = \mu_{PE} + \mu_{Comp} + \mu_{Coh} + ...$$
(2.12)

According to Beer-Lambert law (Als-Nielsen J., 2001), the transmitted photon intensity I_x, is given by,

$$I_x = I_o e^{(-\mu_l x)}$$
(2.13)

where the incident photon intensity is I_o and μ_l is the linear attenuation coefficient. However, using the linear attenuation coefficient (μ_l) has a drawback of varying with the density of the material, hence, the mass attenuation coefficient is used instead and it is obtained as follows,

$$\mu_m = \frac{\mu_l}{\rho}$$
(2.14)

Where ρ indicates the density of material in g/cm^3. Equation 2.13 can be now written as follows:

$$I_x = I_o e^{(-\mu_m \rho x)}$$
(2.15)

In which ρx represents the mass thickness of the target material and specifies its degree of attenuation. Nevertheless, the mass attenuation coefficient has the advantage of being an atomic feature of each element in which it does not alter with changing

the physical state of a given material. For instance, the mass attenuation coefficient is constant for water in the solid or vapor states (Curry *et al.*, 1990; Knoll, 2000).

2.3   X-ray Sources

For the purpose of producing a higher amount of x-rays, a powerful x-ray source is crucial to utilize. An x-ray beam can be produced by three distinct sources: synchrotron radiation, radioactive isotopes and x-ray tubes (Beckhoff *et al.*, 2006). In this study, since x-ray tubes are the only type were used, it will be explained in further detail. X-ray tubes, as shown in figure 2.4, are a combination of several parts, i.e. a heated filament cathode, an empty vacuum, a targeted anode and a high voltage source (Liqiang, 2016).
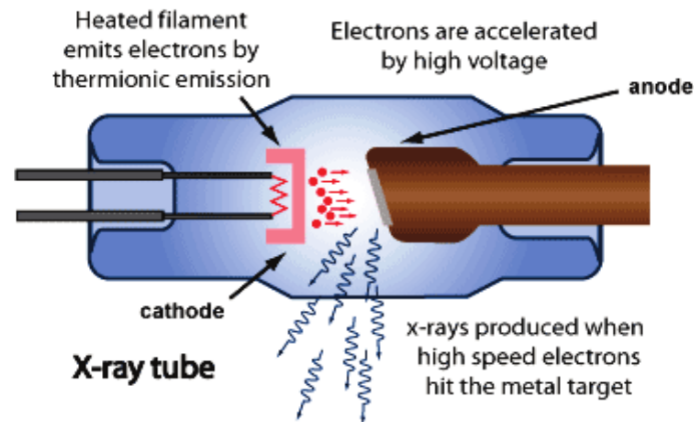
Figure 2.4: X-ray tube diagram showing the mechanism of producing x-rays when applying high voltage between cathode and anode target (Marticke, 2016a).

Electric field exists when applying a high voltage between the cathode and anode material. The cathode is heated and undergoes a thermionic emission process,

releasing electrons. As a result of the applied potential, these electrons attain kinetic energies and accelerate in the direction of the anode target, which can be made of any elemental metal (e.g. tungsten, molybdenum or copper). The interaction that occurs as the electrons strike the anode material will lead the electrons to lose their energy throughout a number of processes (Thayalan, 2014). This study focuses on two physical processes, Bremsstrahlung radiation and characteristic x-rays.
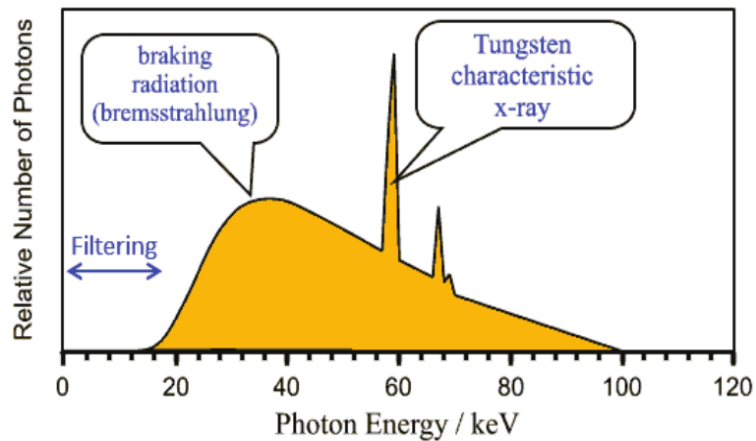
Figure 2.5: An x-ray spectrum of tungsten atom results from emitting bremsstrahlung radiation and characteristic x-rays at 100 kV (Marticke, 2016).

As the emitted electrons are approaching the anode material, they decelerate and lose their kinetic energies in the form of bremsstrahlung x-rays. Owing to the variation in the position of the interaction for bremsstrahlung radiation between the emitted electrons and target nucleus, a broad range of photons will be distributed at different spots as shown in figure 2.5, which corresponds to a continuous spectrum of x-rays. The maximum possible energy of bremsstrahlung or braking radiation to occur is determined by the amount of the voltage applied to the x-ray tube (Als-Nielsen J., 2001). Since distance between the bound electrons and the nucleus is large at the subatomic scale, electrons traverse different distances relative to the nucleus which

Table 2.1: Electron binding energies for W and Mo (Liqiang, 2016).

Electron Shell	Tungsten (W: 74)	Molybdenum (Mo:42)
K	69.5	20.0
L	12.1-10.2	2.9-2.5
M	2.9-1.9	0.60-0.23

changes the energy of the bremmstrahlung emitted. Higher energy bremmstrahlung results when the electron travels close to the nucleus.

The second process in which the accelerated electrons losses their energy is the emission of characteristic x-rays. Figure 2.5 exemplifies the resulted spectrum of this process. If the incoming electron has a higher energy than the binding energy of the anode electrons, an orbital electron may eject resulting in a vacancy in the inner shells. After the atom reaches an excited state, another electron from a higher orbital shell will transmit to fill the created vacancy and a characteristic x-ray will be emitted as a consequence of this transition. Nevertheless, if the incident electron has a lower energy than the binding energy of the target electrons, the bombarded atom will stay stable and no characteristic x-rays will be produced. It should be noted that the intensity of the emitted characteristic x-rays lines is proportional to the increase in the applied voltage (Beckhoff et $al.$, 2006). Table 2.1 presents the binding energies of two commonly used secondary targets, tungsten (W) and molybdenum (Mo).

In order to obtain an x-ray tube spectrum for a tungsten anode as shown in figure 2.6, a filter component is employed to supress lower energy photons (below 20 keV) from the output spectrum (Marticke, 2016a). Another key advantage of utilizing filters when generating x-rays is to diminish the amount of the background radiation (Markowicz et $al.$, 2007).

As the accelerated electrons coming from the cathode are directional towards the
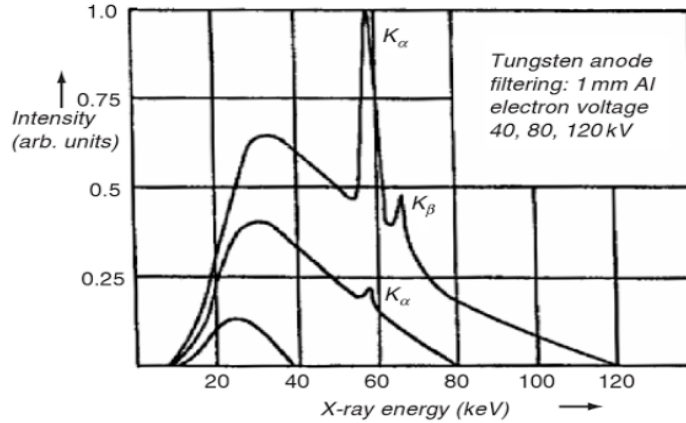
Figure 2.6: X-ray tube output of a tungsten anode target at multiple voltages (40, 80 and 120 kV) incorporated with using aluminum filtering of 1 mm (Beckhoff *et al.*, 2006) .

anode target, this stream of electrons can lead to significant increase in heat and reduction in the number of obtained x-rays. To overcome this drawback, x-ray tubes are mostly including with a rotating anode target (Als-Nielsen J., 2001).

2.4   Non-Destructive X-ray Investigation Techniques

2.4.1   X-ray Fluorescence Techniques

The fundamental principle on which the X-ray fluorescence techniques are based is the photoelectric absorption phenomenon. The photoelectric effect involves interaction between the incident x-ray beam and the electron orbitals in the targeted atom. The transition process that occurs between the orbitals, in order to fill the vacancy of the ejected electron and reach a stable atomic state, cause the emission of characteristic x-rays. As such, experiments that undergo XRF spectrometry are designed on the basis of maximizing the photoelectric effect in the target specimen. In addition to

increasing the probability of the photoelectric effect, preventing the detection of scatter is also another factor to be considered when designing XRF experiments. This is because the scattering events produce high levels of background radiation at the same energy as the characteristic x-rays, which can obscure the actual elemental peaks in the spectrum. Experiments in different fields have been performed using XRF spectroscopy for numerous applications (Heckel *et al.*, 1991; Alvarez *et al.*, 2007; Silva *et al.*, 2012a).

One of the objectives of this study was to highlight the performance of two different X-ray fluorescence spectrometers through the quantification of trace elemental concentrations in healthy and cancerous breast tissues. The two types of XRF spectrometers that have carried out this experiment are the Huber Diffraktionstechnik (referred to as the Huber monochromatic spectrometer) and the polarized energy dispersive XRF spectrometer (PEDXRF). A number of studies that have been conducted using a monoenergetic x-ray target have validated this technique's effectiveness in diminishing scatter events (Alvarez *et al.*, 2007; Farquharson *et al.*, 2013). Though, it should be mentioned that employing a monoenergetic source complicates the process of exciting multiple trace elements in a specimen within a short time. For instance, in the present experiment, a molybdenum target was used to excite elements within the desirable energy range; since molybdenum has a greater energy to cause atomic excitation. Therefore, in order to overcome this drawback, a polychromatic source can be utilized as an improved alternative for exciting multiple elements simultaneously.

The basis of employing a polychromatic source is considered to be paramount to perform EDXRF experiments for interrogating multiple elements simultaneously. If the condition is to examine an individual element, then an x-ray energy barely

higher than the binding energy can be used to increase the probability of inducing an emitted characteristic x-rays. While the EDXRF technique is characterized by simultaneously identifying multiple trace elemental compositions over a wide range of concentrations, it has the disadvantage of containing increased scatter in the spectrum (Beckhoff *et al.*, 2006). Hence, a number of recent studies have shifted towards incorporating a polarized x-ray beam while implementing EDXRF experiments which leads to PDEXRF technique (Zhan, 2005; Marguí *et al.*, 2006; Abuhani *et al.*, 2014). The features of rejecting scatter events and producing more characteristic x-rays, can be accomplished by utilizing a powerful x-ray tube accompanied by using a suitable type of secondary targets in a Cartesian or tri-axial configuration. This can lead to an improvement in the signal-to-noise (S/N) and the minimum detection limits (MDLs), i.e. the minimum concentration or quantity for an element to be measured within a given material (Markowicz *et al.*, 2007).

Incorporating a polarized beam while employing a Cartesian setup will result in polarizing the beam towards the sample, which in turn plays a key role in diminishing the scatter beam incident on the detector. This advantage provides the opportunity for using a powerful x-ray tube which reduces the measurements' acquisition time. The characteristic x-rays emitted from a specimen are not polarized and can travel in all directions; including the one towards the detector. As a consequence, utilizing a polarized beam will only result in reducing the scattered photons incident on the detector but will have no impact on the number of the produced characteristic x-rays.

An x-ray beam may scatter perpendicularly on a plane only if the electric field vector of the incident beam has a component at an angle of 90° to the scatter plane
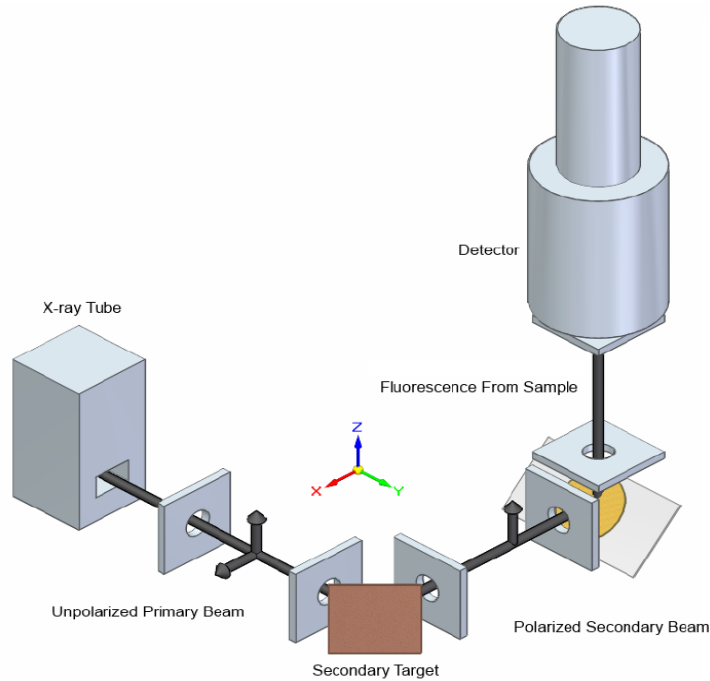
Figure 2.7: The PEDXRF configuration, indicating the polarization vectors of the primary and secondary beams (Johnston *et al.*, 2017).

(Heckel *et al.*, 1991). This can be explained through the configuration scheme presented in Figure 2.7. The beam from an x-ray tube is unpolarized, hence at a given angle of 90°, the x-ray tube output can be described as the sum of two perpendicular polarization vectors , $\overrightarrow{E_x}$ and $\overrightarrow{E_z}$. The primary beam is then scattered off of a secondary target, which is used to excite photons within a sample, leading to the production of a secondary beam. The sample is positioned perpendicular to the original beam direction, and the secondary beam is polarized towards the $\overrightarrow{E_z}$ direction; since the polarized beam in the $\overrightarrow{E_x}$ direction cannot scatter in the direction of the sample (Heckel *et al.*, 1991, 1992; Als-Nielsen J., 2001; Johnston, 2017). The detector will therefore detect no scatter events from the primary beam, however, only the emitted characteristic x-rays will be detected from the specimen; as the detector is positioned

in a perpendicular direction to both the primary and secondary beams.

In order to increase the intensity of a polarized beam, certain considerations need to be taken when designing a PEDXRF experiment. Choosing an appropriate secondary target material is essential to polarize the primary x-ray beam. Secondary targets are classified into three main types (i.e. Barkla scatterers, Bragg polarizers and metallic fluorescers). For measuring biological samples, metallic fluorescers secondary targets are the most suitable and effective type to use. Since the study's objective was to evaluate the performance of two different XRF systems through the investigation of trace elemental compositions, a molybdenum secondary target was selected to conduct these experiments. This is because a molybdenum target produces characteristic x-rays with a higher energy than the binding energy of the elements of interest. As the secondary target polarizes the primary beam, but results in non-polarized characteristic x-rays, this drawback will enable the produced characteristic x-rays to scatter towards the detector. However, this consequence is minor when looking at the improvement of the photoelectric effect likelihoods (Heckel *et al.*, 1991; Johnston, 2017). Besides employing a suitable type of secondary target, the collimator's design is also another important factor to consider when performing PEDXRF experimentations (Heckel *et al.*, 1991).

2.4.2   X-ray Diffraction Techniques

The process of investigating biological samples, along with the use of XRF techniques, can become more promising when combined with x-ray diffraction spectroscopy (XRD). While XRF spectroscopy is able to provide information on the

elemental composition of a specimen, XRD spectroscopy enables one to obtain information on the structural components. As such, combining these two spectroscopy methods may ensure accurate results are achieved on the material of interest.

XRD technique is based on coherent interaction; when an x-ray beam passes through a material, it interacts with the electron clouds of the atom and causes the electrons to oscillate. The movement of electrons leads to the emission of photons at the same wavelength of the incident beam. As a consequence, interference patterns that occur between the scattered photons off a material leads to XRD phenomena(Als-Nielsen J., 2001; Theodorakou and Farquharson, 2008). The constructive interference that occurs between the scattered photons at determined angles θ, will result in producing x-ray diffraction patterns or Bragg's effect. An illustration of this effect is given in Figure 2.8. Bragg angle,θ_B, at which the interference takes place between the waves, x-ray wavelength, λ, and the interplanar distance d, is found in equation 2.16.

$$n\lambda = 2dsin\theta_B \qquad (2.16)$$

Where n represents an integer and indicates the reflection order or the path difference.

Furthermore, the observed interference patterns between the scattered photons are governed by the phase difference of these photons. As the two photons are emitted at the same wavelength, the phase difference is correlated to the path difference in which the two photons traversed through a material. A constructive interference will result if Bragg's condition is satisfied as presented in the equation 2.16. However, a destructive interference will result on the condition that the incident wavelength is not a half-integer number. As the material type impacts the diffraction patterns, highly
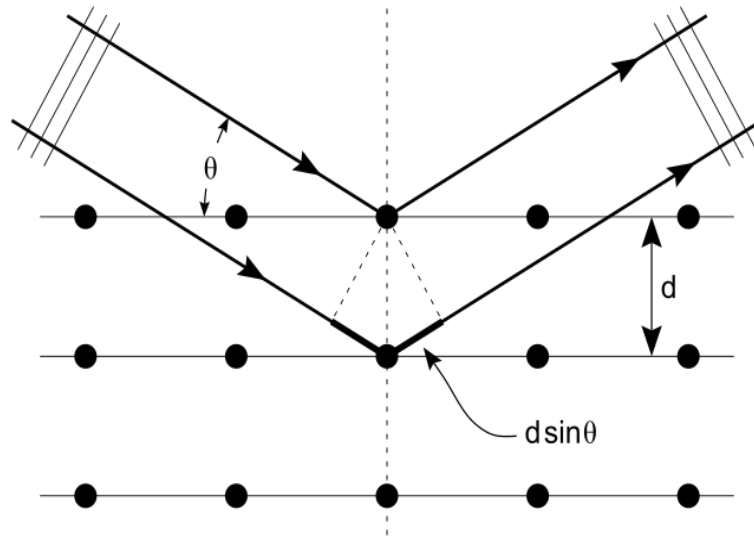
Figure 2.8: Braggs condition is displayed in which the path difference corresponds to $2dsin\theta_B$.

ordered materials such as crystals and powders are the most straightforward types for conducting XRD experiments. While in the case of less ordered or amorphous materials like biological specimens, observed XRD patterns are less discernable. This is due to the fact that crystals have an arrangement of atoms that exist in long repetitive patterns, in which the inter-atomic spacing, d, between the neighborhood atoms is equal. Where homogeneous materials exist in short range patterns; and therefore, their inter-atomic spacing tend to vary (Als-Nielsen J., 2001). This inconsistency in the space between the atoms gives rise to broader and less prominent diffraction patterns. The inter-atomic spacings are present in the atom as a collection of spacings in three dimensions. Furthermore, in the case of crystallography, inter-atomic spacing can be determined by Miller indices as they have long range of reproducibility (Marticke, 2016). Whereas, inter-atomic spacings of biological samples can be calculated as the average spacing of separate inter-atomic spaces aligned in the same direction. Determining the inter-atmoic spacings of a material can be accomplished using two

different modalities of XRD spectroscopy; EDXRD and ADXRD.

With the Energy Dispersive X-ray Diffraction (EDXRD), constructive interferences of diffraction patterns are measured across a range of energies via a polychromatic X-ray source while keeping the scattering angle fixed. Figure 2.9 displays an example of EDXRD experimental setup. As demonstrated in equation 2.16, this indicates that constructive interference patterns will only take place at determined wavelengths (and hence energies) as the scattered angle is fixed. As such, perform-
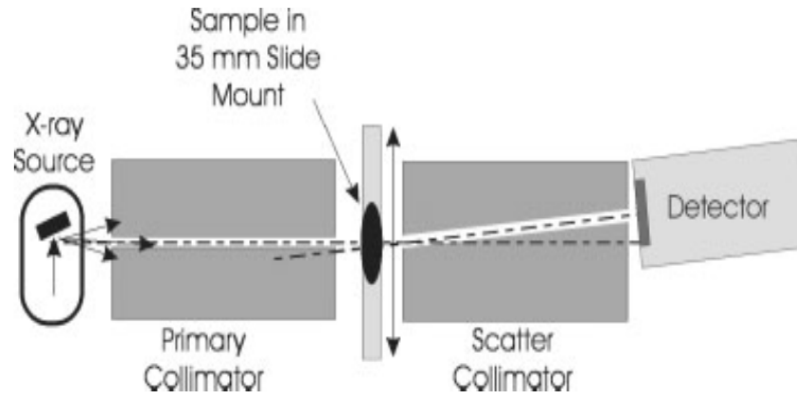
Figure 2.9: EDXRD experimental setup (Farquharson and Geraki, 2004).

ing EDXRD has the advantage of preserving time since the experiment geometry is stationary and the utilized x-ray source is polyenergetic.

EDXRD experiments require a strict collimation design in which the polychromatic X-ray source must be monodirectional towards the sample. Collimating the primary incident beam is essential to define the beam path within a specimen. Afterwards, a scatter collimator is employed to establish the scattering angle. As the scatter collimator contains various slit collimators, a number of scattering angles can be determined.

34

On the other hand, in the Angular Dispersive X-ray Diffraction (ADXRD), the X-ray energy beam is monochromatic and the scatter intensity is measured as a function of the incident X-ray angle. This indicates that constructive interference patterns will arise at specific angles since the beam energy is fixed, and hence, atomic spacings can be calculated. Obtaining a variety of incident beam angles can be achieved by moving the experimental configuration during data acquisition (i.e. the x-ray source or detector). ADXRD therefore clearly, has the disadvantage of longer measurement times when collecting data. Despite both of the previously mentioned XRD methods being capable of measuring molecular structure, it should be mentioned that EDXRD has some downsides when used. For instance, the increase in background noise which is attributed to the detection of compton scattered and characteristic x-rays. In addition, EDXRD involves calibrating the x-ray source intensity at different energies with the aim of making results comparable to other XRD techniques (Marticke, 2016b; Johnston, 2017).

For the purpose of comparing results of different XRD modalities, the momentum transfer is used and given by (Als-Nielsen J., 2001):

$$x^2 = k^2 + k^{'2} - 2kk^{'}cos\theta \tag{2.17}$$

Where k and $k^{'}$ are the wavenumbers of the incident and scattered photons respectively. In the case of coherent scattering process, $k = k^{'}$ and hence equation 2.17 can be reduced to:

$$x = 2ksin\frac{\theta}{2} \tag{2.18}$$

For spectroscopic studies, the momentum transfer term, which is expressed in units

of nanometre inverse (nm^{-1}), can be defined again as follows:

$$\chi = \frac{1}{\lambda}sin(\frac{\theta}{2}) = \frac{E}{hc}sin(\frac{\theta}{2}) \qquad (2.19)$$

Where E is the x-ray energy, h, c are Plank's constant and the velocity of light respectively, λ is the wavelength of the incident photon and θ is the angle in which the photon is deflected through. Therefore, momentum transfer facilitates the comparison between EDXRD and ADXRD, since it combines the variables of interest, i.e. incident energy and angle.

Chapter 3

Methodology

This chapter presents the methodology and techniques which were performed in the present study. A set of 19 matched-pairs of breast samples were collected to conduct this experiment. Once the samples were prepared following a certain procedure, a total of four sets of data were obtained using two different X-ray detection systems, as each system encompasses two dissimilar X-ray techniques: X-ray Fluorescence and X-ray Diffraction. After the data were collected from both systems, each set of data was fit in order to obtain the elemental concentrations and the structural components of the examined breast tissues. Different data fitting and normalization procedures were followed in order to make the comparison of the established data from both of the X-ray detection systems meaningful. The following step was to analyze the obtained information to observe any differences in terms of the tissues elemental composition and structural components of the investigated specimens. Further details about the implemented procedures are presented below.

3.1   Sample Preperation

In order to evaluate the performance of the two X-ray detection systems, a particular procedure was followed to prepare the breast specimens. A set of nineteen matched-pairs of breast tissues were obtained from the Ontario Tissue Bank (OTB) from nineteen different breast cancer patients. This collection of matched-pairs constituted of invasive ductal carcinoma (IDC) of breast and normal surrounding breast tissues. A storage process was followed so that the specimens were stored at -85° and kept frozen until the measurement time in order to prevent them from degeneration. At the measuerment time, the specimens were defrosted in a laminar flow cabinet and mounted into octagon sample holders using sterile surgical scalpel handles and blades. The sample holders were 3D printed out and fabricated from Polylactic Acid (PLA) with 25.4mm width and 10.3mm side length. As displayed in Figure 3.1, holes of 1mm thickness and 12.7mm diameter exist in the center of the sample holders to position specimens into them. Once the breast sample was placed onto its designated holder, the sample was then covered by 4-μm-thick XRF Ultralene film in order to seal it in place.
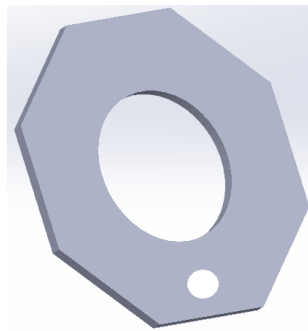
Figure 3.1: Computer rendering of the sample holder used in the entire experiment.

As those samples were measured using four different X-ray techniques, once a required spectrum was obtained from a sample using any of those techniques, the sample was returned to the laboratory freezer until the time of initiating the next set of measurements.

3.2   X-ray Fluorescence Set-up and Measurements

As the main purpose of the present experiment was to evaluate the effectiveness and accuracy of the two previously mentioned X-ray detection systems, a preliminarily study was performed to assess their XRF detectors through the quantification of trace elemental composition for Cl, K, Ca, Fe, Cu, Zn, Br and Rb in the earlier mentioned breast specimens set.
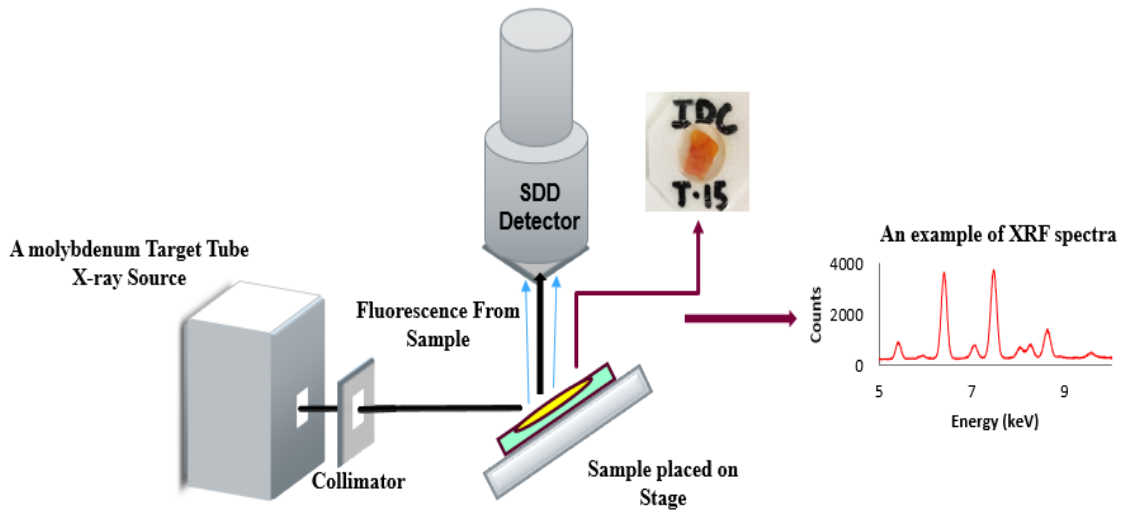
Figure 3.2: The conventional XRF experiment configuration, demonstrating the data collection set-up.

In the Huber XRF spectrometer, shown in Figure 3.2, the X-ray source is a molybdenum target that is monochromated to 17.44 keV and focused to deliver a

$1.8mm \times 1.8mm$ beam of approximately 3.5×10^6 photons per second on the sample.

At the time of measurement, the sample was angled at 45° and a silicon drift detector (SDD) with an active area of $150mm^2$, was positioned at 90° to the incident beam and used to collect spectra. Achieving this angle for the sample was fulfilled through the use of a solid cylinder that has a 45° angle cut-out. This solid cylinder possesses a hole in the center. By looking again at Figure 3.1, the small hole at the bottom of the sample holder was used to secure the sample holder on
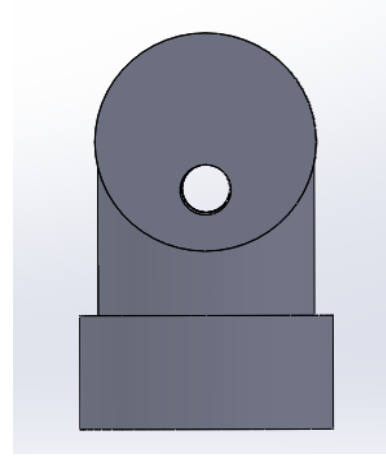
Figure 3.3: A solid cylinder angled at 45° was used to position samples during data collection.

the solid cylinder by inserting a small nail through the holes. Figure 3.3 illustrates the design of the solid cylinder for positioning samples. The X-ray tube parameters were $50kV$ and $500\mu A$, and data were collected for 30 minutes per specimen.

In contrast to the Huber XRF system, the PEDXRF system elaborated in the previous chapter and shown in Figure 2.7 utilizes a polarized beam while implementing the XRF experiment, which contributes to a significant reduction of X-rays scatter. The PEDXRF system, unlike the Huber XRF system, has the advantage of employing different types of secondary targets (i.e. copper, zinc and molybdenum) to excite a specific element or a set of different elements. Positioning the secondary target as well as the sample holder at a 45° angle was accomplished through use of a 3D designed block shown in Figure 3.4 (Johnston, 2017). Since the current experiment of XRF focused on analyzing elements in a given range of energy as presented in Table 3.1,

molybdenum was selected as an optimal secondary target for this system.
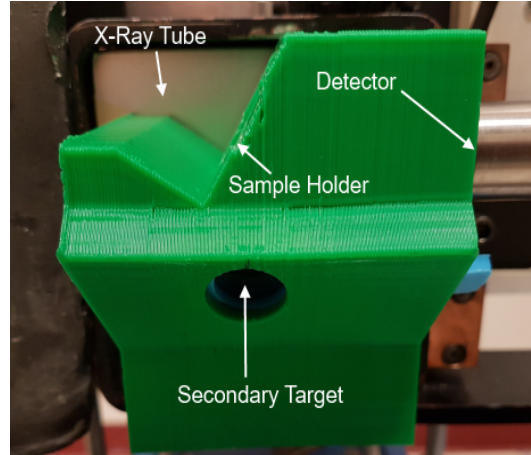
Figure 3.4: A 3D printed out block fabricated from PLA was used to mount the sample and secnodary target during the measuerment.

To ensure the beam irradiates the sample only, the collimators used in this system were designed to match the size of the sample holders holes. The X-ray tube was set to 50 kV and 25 mA. Spectra were collected for 10 minutes per sample, with the emitted beam corresponding to an elliptical shape that allows irradiation of most of the sample. A comparison of the beam size between the Huber XRF system and the PEDXRF system (Johnston, 2017) is shown in Figure 3.5. Collecting spectra obtained from samples was achieved using a SDD as well, with an active area of $150mm^2$.

3.2.1   Data Fitting

A total of 76 XRF spectra (38 spectra of matched-pairs samples obtained from each XRF system) underwent a fitting process in order to obtain quantitative information regarding elements of interest. The fitting procedure was implemented through the use of a matlab code that was developed by Eric Johnson (a former group member).
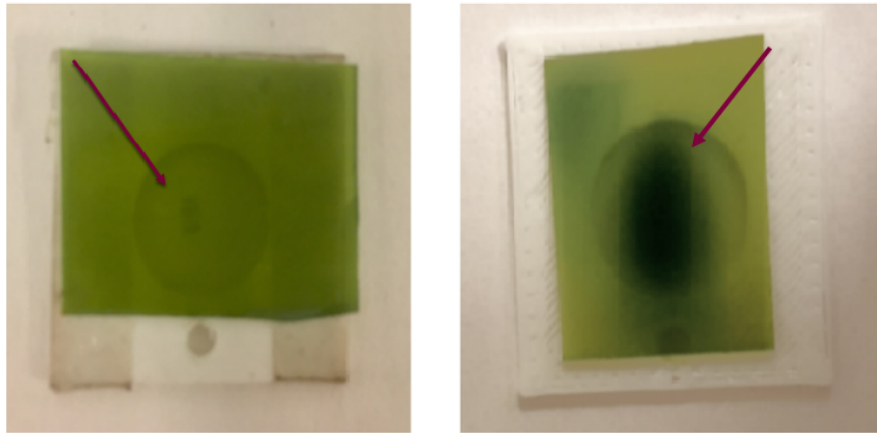
Figure 3.5: Two radiochromic x-ray films, show the beam size of the Huber x-ray tube on the left, and the PEDXRF beam size on the right.

Each spectrum was divided into three regions of interest (ROI) as shown in Table 3.1 to be able to obtain accurate information about each $K\alpha$ photopeak associated with each element of interest (BEARDEN, 1967). A fourth area of interest, which represnts the scatter regions, was also included in the fitting.

Table 3.1: Elements in Different ROI

First ROI	$K\alpha$ (keV)	$K\beta$ (keV)
Cl	2.62239	2.8156
K	3.3138	3.5896
Ca	3.69168	4.0127
Second ROI	$K\alpha$ (keV)	$K\beta$ (keV)
Fe	6.40384	7.05798
Cu	8.04778	8.90529
Zn	8.63886	9.5720
Third ROI	$K\alpha$ (keV)	$K\beta$ (keV)
Br	11.9242	13.2914
Rb	13.3953	14.9613

Prior to fitting each measurement, a background subtraction was executed for precisely determining fluorescence signal. A smoothing procedure was also incorporated

into the code in order to suppress any statistical fluctuation that may emerge from the contents uncertainty of each channel. Subsequently, each fluorescence photopeak corresponding to the element of interest was fitted with the associated Gaussian and the integrated area was afterward determined.

With the aim of performing a comparative analysis between the two XRF systems, and to account for any variation in the X-ray source flux and time of measurement, in addition to the difference in samples thickness, it was decided that normalizing the integral area of each fluorescence peak to the total scatter peak area is the most suitable normalization factor. Furthermore, the difference in samples thickness revealed detecting higher scattered photons in thicker samples when compared with thinner ones. While each detected $K\alpha$ fluorescence emission is related to the elemental concentration of each correspnding element in the specimen, total scatter peak may result from the scattering of the incident X-ray beam by the sample. Therefore, calculating the area using the ratio of the fluorescence peak to the total scatter was intended to provide accurate elemental composition of an investigated specimen.

3.2.2   Statistical Analysis

The obtained data sets from the two XRF systems were analyzed statistically to evaluate the trace elemental composition of the examined samples. To perform the statistical analysis, IBM SPSS Statistics (Version 22) was employed. Descriptive statistical analysis was completed to deduce statistical variables including mean, standard error and standard deviation. The Shapiro-Wilk test was used to determine whether the observed data set followed a normal distribution. For non-normally distributed data, nonparametric Wilcoxon signed-rank test was used to assess the differences among

variables. As an alternative to that, and in order to examine the significant param-
eters for normally distributed data, a Paired-Samples T-Test with a 95% confidence
interval was used.
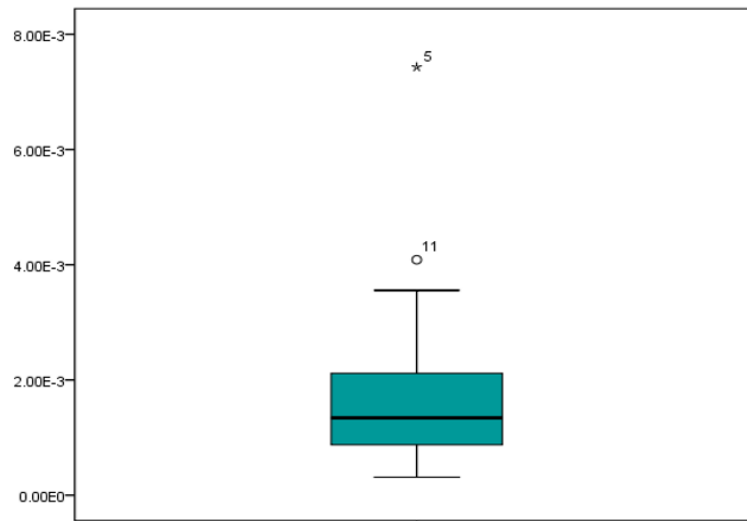
Figure 3.6: An example of a boxplot indicates the five values of interest.

For the purpose of optimally displaying the distribution of the observed data, box-
plots were introduced. Visualizing data using boxplots is based upon presenting five
values: the minimum, the interquartile range (i.e. including first and third quartiles),
the median, and the maximum. An example of a boxplot is given in Figure 3.6. The
interquartile range (IQR) represents the rectangular box in the center and compasses
the first quartile to the third quartile (Q1 to Q3). The horizontal line inside the box
indicates the median value, while the outline lines or "whiskers" indicate the mini-
mum and maximum values. The blank circles refer to potential outliers which can be
defined as any values higher than 1.5 multiplied by IQR, whereas other values greater
than 3 multiplied by IQR are plotted as asterisks and are considered outliers.

3.3   X-ray Diffraction Set-up and Measurements

The second objective of this study was to highlight the features and discrepancies between each XRD spectrometer incorporated in both systems by investigating the structural components (i.e. adipose, fibrous and water) of the same aforementioned breast tissues. As mentioned earlier, the conventional monochromatic X-ray system (or the Huber) encompasses an ADXRD detector besides the XRF detector.
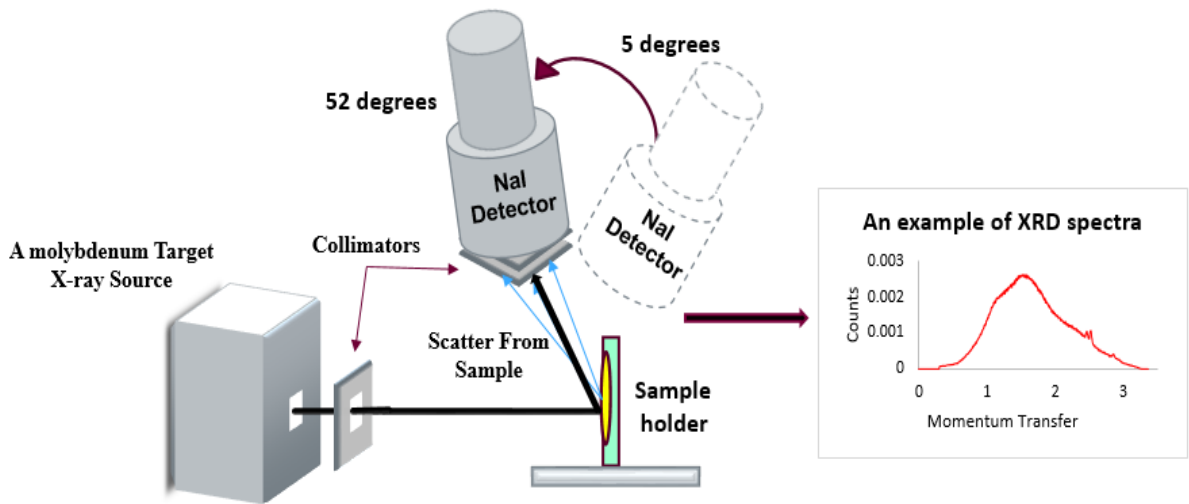
Figure 3.7: The experimental setup of ADXRD.

A schematic for the ADXRD experiment configuration is presented above. The employed detector was a sodium iodide (NaI) crystal with $2mm \times 2mm$ collimation. As performed with the Huber XRF measurements, during the ADXRD measurements, the sample holder was placed onto a stage using a different sample mount and secured in place by inserting a nail through the small hole in the bottom of the sample holder. Figure 3.8 illustrates the sample mount used in this experiment. Each breast specimen was measured on a range of angles from 5° to 52°. Furthermore, samples were measured starting from 5° to 25° at 0.5 interval step, and then from 28° to 52°

in steps of 3°.

This setup was chosen as the investigated specimens would ideally reveal structural components between 5° and 24.5° which correspond to 0.618 and 3.01 nm^{-1} respectively. However, following this range, there are no significant structural details to be obtained; consequently, an interval step of 3° was decided in an effort to shorten the time of measuring. Since the ADXRD technique is incorporated with the conventional monochromatic system, and hence utilizes a fixed energy, it required at least 60 minutes per sample to obtain data in this experiment. On the other hand, with the EDXRD

Figure 3.8: The sample mount used to secure sample holders onto a stage during ADXRD measurements.

technique the scatter intensity is measured across a range of energies using a polychromatic X-ray source while keeping the scattering angle fixed. Therefore, the former technique provides the advantage of collecting data in a short time frame (i.e. 10 minutes per measurement).

The EDXRD detector used was an ORTEC High-Purity Germanium (HPGe) detector with a crystal diameter and length of $25mm$ and $13mm$ respectively. The experimental set-up of this technique is previously presented in Figure 2.9. The x-ray beam traverses through a $2mm$ aluminum filter which aims at suppressing undesired low energies from the primary beam. Since this method imposes a strict collimation, the beam after that passes through a primary lead collimator with a $1mm$ slit width and $10mm$ height, which intends to focus the beam path towards the sample. The sample is placed in a sample holder that is adjacent to the primary collimator

opening. The resultant beam will then travel across a scatter collimator representing an aluminum block as shown in Figure 3.9 (Johnston, 2017). This block constitutes multiple angles ranging from 3° to 13° with $1mm$ slits to achieve optimal results at desired angles. In order to obtain precise information from interrogated samples and to suppress any unwanted energy photons from being detected, supplemental collimators were added to the end of the angle block.
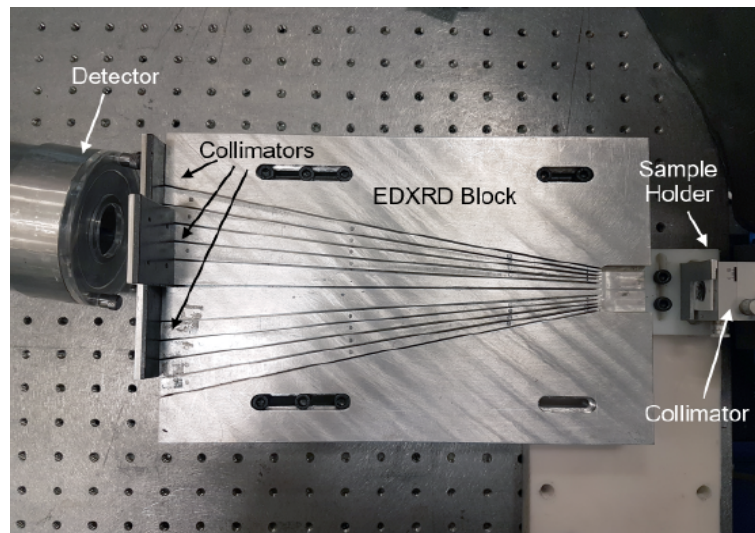
Figure 3.9: The EDXRD system set-up. All components are installed on an optics table to ensure the system stability while measuring samples.

For the present experiment, a tungsten x-ray tube was employed and operated at $80kV$ and $8mA$ with a diffraction angle of 6°. This angle was chosen as it provided an optimal result for the examined breast tissues in the range of $0.58nm^{-1} - 2.41nm^{-1}$. As this technique provides the advantage of collecting data in a shorter time period, each sample underwent four measurements at four different edges as shown in Figure 3.10. Using an octagon shaped sample holder was, therefore, advantageous to easily rotate each sample in the sample holder used in this system. This approach of the experiment was implemented to test the homogeneity of the examined samples.
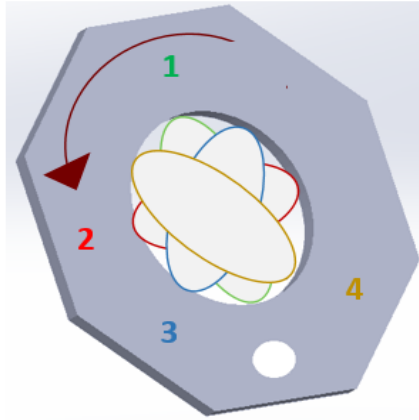
Figure 3.10: Computer rendering to the beam shape while rotating the sample. To help to visualize, each measuered beam is labeled with a different number and color.

For the purpose of aligning the expected diffraction peaks from breast specimens, four different types of samples were used. These samples were chicken breast, deionized water purchased from VWR International, calcuim carbonate ($CaCO_3$) and lard. These samples were selected based on the assumption that they possess similar properties to the contents of examined breast specimens. Furthermore, chicken breast was chosen as it is composed of a similar structure to a breast tissue, while lard and water were selected to assign adipose and water peaks respectively. $CaCO_3$ is found abundantly in living organisms and their environments. It is also characterized by having highly ordered structure, and therefore gives rise to a definitive diffraction profile. A similar sample preparation procedure as presented in section 3.1 was applied to this samples set. However, for the deionized water, the sample holder was covered first by the x-ray Ultra film which was secured using silicone. Following this, the deionized water was injected into the sample holder by using a small needle. Each one of these samples was measured via the EDXRD detector for 10 minutes, using the same previously mentioned X-ray tube operation sittings. The obtained diffraction patterns

are shown in Figure 3.11.
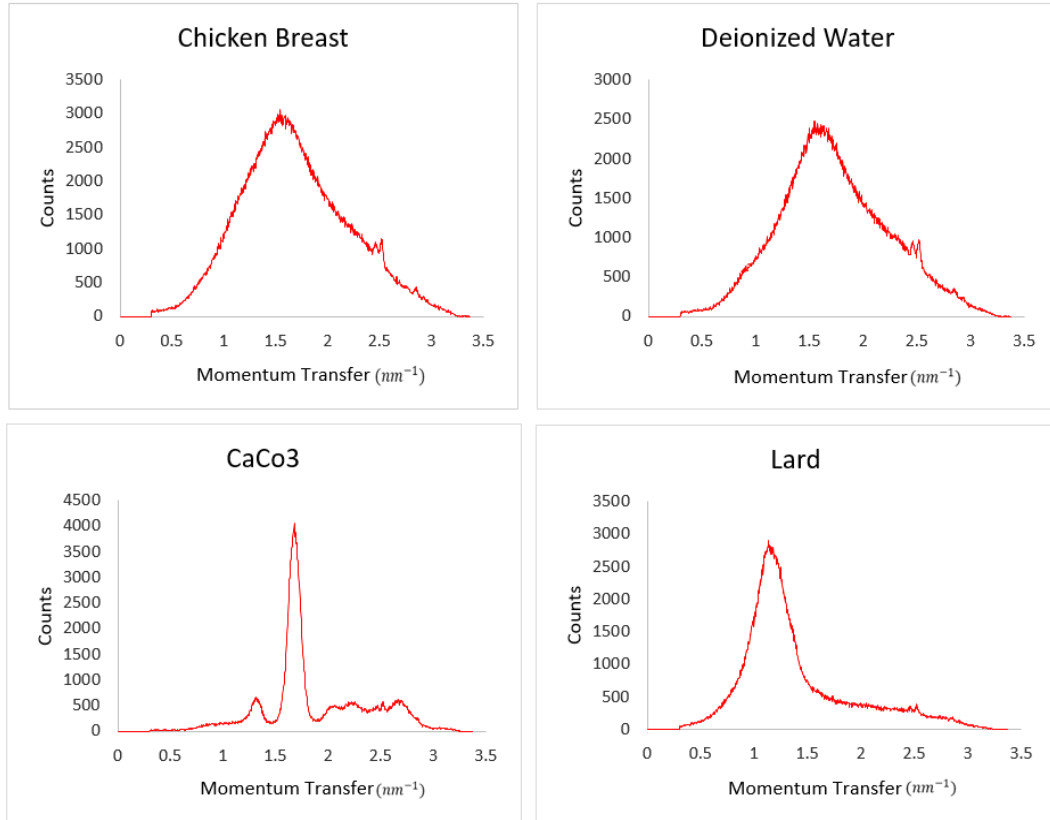
Figure 3.11: The foreseen diffraction patterns from four different types of samples.

As demonstrated in Figure 3.11, the chicken breast is substantially homogeneous in the fibrous content corresponding to a diffraction peak at $1.6 nm^{-1}$. The same peak can be seen in the deionized water spectrum, as this peak arises from insoluble uncharged fibers in the sample. In addition to the fibrous peak, another peak is clearly revealed at $2.2 nm^{-1}$ for both chicken breast and deionized water samples, this peak corresponds to the water content. Predominant adipose and fibrous peaks are shown in the lard and $CaCO_3$ spectra at $1.1 nm^{-1}$ and $1.6 nm^{-1}$ respectively.

3.3.1   Data Fitting

In order to obtain a quantitative characterization for the diffraction profiles resulting from the examined breast specimens using both ADXRD and EDXRD, a proper fitting procedure has been followed. The collected diffraction profiles were analyzed by using PeakFit^{TM} Software Version 4.06 SPSS Inc. A smoothing procedure was performed using Savitzky-Golay algorithm to eliminate channels statistical fluctuation. Following this, a background subtraction step aimed at obtaining accurate signals of diffraction peaks was taken prior to fitting each spectra. Each diffraction peak was afterwards adjusted with its corresponding Gaussian amplitude peak to determine the associated integrated area. The fitting technique followed with EDXRD and ADXRD scatter profiles is presented in Figure 3.12 (Ryan and Farquharson, 2007).
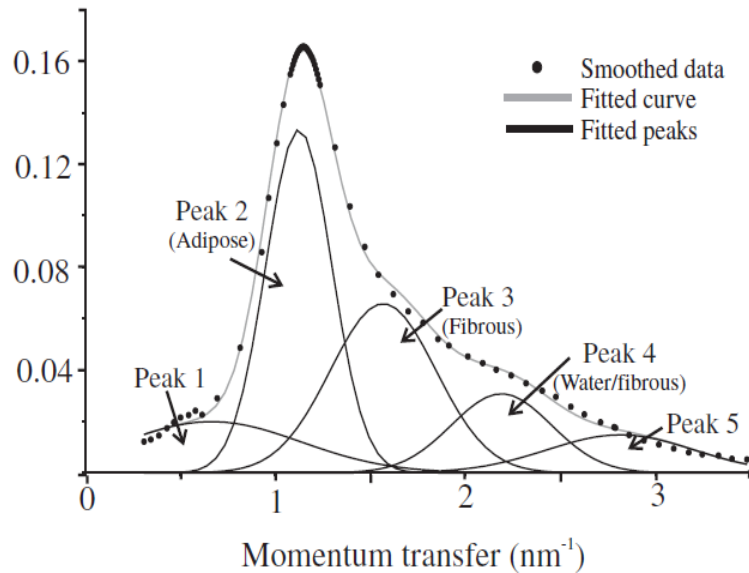
Figure 3.12: The used diffraction model to fit the obtained diffraction data from both XRD systems.

With respect to the diffraction profiles, two normalization methods were applied.

First, since more counts were extracted from the EDXRD system, and with the goal of making the obtained data and plots comparable between the two diffraction systems, each obtained spectrum was normalized to the highest peak content; so the maximum peak is equal to one following normalization. This method also accounts for the change in the X-ray source flux and difference in time of measurement between the two systems. Secondly, in order to evaluate the results of each diffraction system separately, the data set of each system was normalized to unity. This procedure as before aimed at eliminating the change in the X-ray source flux and intensity. Analysing the diffraction data statistically was performed in a manner similar to that mentioned in subsection 3.2.2.

Chapter 4

Results and Discussion

After stating the purpose of the present study, and the various methods and approaches that were followed to obtain our results, this chapter will present the acquired statistical results from the different applied techniques. Moreover, a comprehensive comparison study was performed to highlight the results achieved from both of the Huber X-ray detection techniques for XRF and ADXRD, and the combined PEDXRF and EDXRD detection system. In addition to the previously mentioned comparison studies, the reproducibility of both aforementioned systems was also tested to demonstrate the accuracy and reliability of each system for examining biological specimens.

4.1   X-ray Fluorescence Comparison Study

Trace elements play a significant role in metabolic and other vital processes in the human body, and adopted widely to indicate the pathogenesis of various morbid diseases such as breast cancer. Accurate, reliable and rapid results are required when investigating biological specimens, which in turn expedite diagnosis and treatment.

As our primary goal was to evaluate the performance of the Huber XRF and the PEDXRF techniques, the concentrations of elements of interest demonstrated in the previous chapters were statistically analyzed. Deducing the concentration of each element was accomplished by determining $K\alpha$ photopeaks corresponding to elements of interest. For instance, the emission of a $K\alpha$ characteristic X-ray is directly proportional to the number of atoms correlated to the examined element. Two examples of the expected spectra prior to background subtraction are shown below in Figures 4.1 and 4.2. These spectra represent the averaged counts of the interrogated tumor breast samples using both aforementioned XRF systems. Averaging the counts of the cancerous breast specimens was decided to aid in depicting the content of elements of interest.
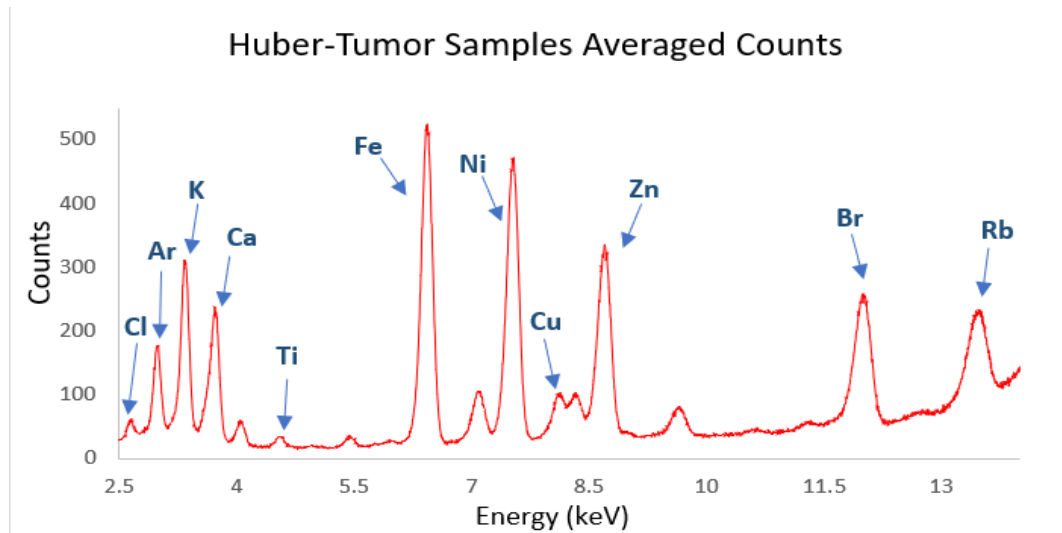
Figure 4.1: Emission of X-rays characteristic of examined elements are indicated by arrows.

The $k\alpha$ emission lines associated with trace elements involved in the present study are indicated by arrows in Figures 4.1 and 4.2. While other emission lines are not indicated in these figures either they are correlated to $k\beta$ or they represent other
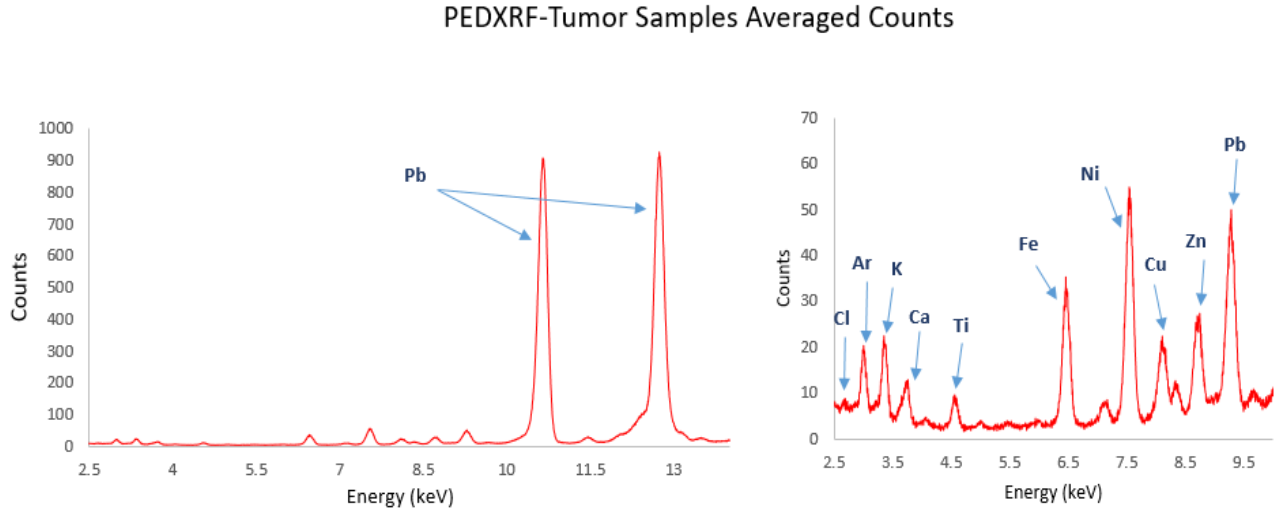
Figure 4.2: The emission of characteristic lines of elements is shown on the left. The range of energy between 2.5keV-10keV is enlarged to help to visualize those lines.

elements not included within the scope of this study. In both previous figures, peaks at $2.68keV$, $3.31keV$ and $3.69keV$ correspond to chlorine, potassium and calcium elements. The peaks at $2.96keV$ and $4.51keV$ correspond to argon and titanium respectively. Whereas argon arises due to the air ionization by incoming X-rays, titanium emerges in all of the acquired measurements from the colorant used to color the sample holders. Other peaks at $6.4keV$, $8.02keV$ and $8.63keV$ sequentially correspond to iron, copper and zinc. The nickel peak present at $7.48keV$ in both spectra, is fully resulting from the head of the silicon drift detector, but not the examined specimens. Bromine and rubidium peaks are displayed at $11.92keV$ and $13.39keV$ respectively. By looking at the spectrum in Figure 4.2, three lead peaks are distinctively present at $9.2keV$, $10.5keV$ and $12.6keV$, corresponding to the following emission lines L1, Lα and Lβ respectively. It is hypothesized that the emitted L lines of lead are due to the collimators used to collimate the beam in the PEDXRF system. Furthermore, as evident in chapter two, the PEDXRF system necessitates

strict geometry to focusing the beam path towards the sample, which therefore requires placing several lead collimators. However, these collimators have the drawback of emitting characteristic Lead L-lines when interacting with X-rays. Nevertheless, it is clear that those lead lines do not interfere with any of the characteristic X-rays of investigated elements in this experiment. Another limitation of the materials used to construct the PEDXRF system is the composition of trace elements such as copper. It is assumed that the copper peak mainly arises from the impurities in the aluminum used to filter the beam and the contamination caused by the 3D printing and machining process (Johnston, 2017), which leads to getting absorbed by the detector. Therefore, these considerations should be taken into account when resolving elemental concentrations and comparing between the two XRF systems performance. Due to the utilized molybdenum secondary target, Compton and coherent peaks are presented at $17.44keV$ and $19.6keV$ respectively in the complete spectra for both of the Huber XRF and PEDXRF systems. A distinctive feature of both systems as shown in Figures 4.1 and 4.2 is having approximately equivalent energy resolution for resolving characteristic X-ray peaks corresponding to elements of interest.

Analysing the investigated elements statistically using the aforementioned XRF techniques have revealed statistically consistent results for both detection systems. The achieved statistical results, including elemental median levels in both normal and tumor breast tissues with the associated inter-quartile range (IQR) are presented in Tables 4.1 and 4.2. As the integral areas of the characteristic $K\alpha$ X-rays corresponding to elements of interest were normalized to the total scatter, it is important to note that this normalization procedure aids in making samples measured with different thickness and X-ray tube intensities comparable. A statistically significant

increase in the levels of Fe ($P < 0.05$), K, Ca, Zn and Rb ($P < 0.01$) is noticeable in the cancerous tissue in contrast to the healthy tissue. Nevertheless, the obtained results of Cl, Cu and Br have indicated insignificant difference between the normal and tumour breast tissues. The previous established results are in agreement with the results of (Silva *et al.*, 2009; Siddiqui *et al.*, 2006; Farquharson *et al.*, 2013).

Element	Tissue Type	Median	IQR	P-Value
Cl	Normal	.0003	.0002	$= .117^a$
	Tumor	.00019	.00008	
K	Normal	.0009	.0005	$<0.01^{*a}$
	Tumor	.002	.002	
Ca	Normal	.0010	.0003	$<0.01^{*a}$
	Tumor	.001	.001	
Fe	Normal	.002	.002	$<0.05^{*a}$
	Tumor	.004	.005	
Cu	Normal	.0006	.0003	$= .091^a$
	Tumor	.0005	.0002	
Zn	Normal	.001	.001	$<0.01^{*a}$
	Tumor	.003	.004	
Br	Normal	.002	.001	$= .059^a$
	Tumor	.003	.003	
Rb	Normal	.0007	.0005	$<0.01^{*a}$
	Tumor	.002	.002	

Table 4.1: The statistical results of the Huber XRF system for the elements involved in this experiment. Tissues classifications, number of samples (N=19) and statistical values between normal and tumor breast specimens are seen in the table.
[a] Wilcoxon Signed Ranks test.
[*] Significance tested at $P < 0.05$

In order to visually observe the statistical results and distribution of data sets of the XRF utilized systems, box plots are displayed in Figures 4.3 and 4.4 showing the range, median and inter-quartile range (IQR) of each examined element. It can be seen that, both data sets obtained from both XRF systems include outliers and strikes. This variation in elemental concentrations of samples suggest that further

Element	Tissue Type	Median	IQR	P-Value
Cl	Normal	.0001	.0001	$= .057^a$
	Tumor	.00005	.00009	
K	Normal	.0006	.0002	$<0.01^{*a}$
	Tumor	.002	.001	
Ca	Normal	.0007	.0003	$<0.01^{*a}$
	Tumor	.0009	.0007	
Fe	Normal	.002	.002	$<0.05^{*a}$
	Tumor	.003	.002	
Cu	Normal	.003	.001	$= .227^a$
	Tumor	.002	.0008	
Zn	Normal	.0012	.0009	$<0.01^{*a}$
	Tumor	.003	.003	
Br	Normal	.00006	.00016	$= .053^a$
	Tumor	.0001	.0003	
Rb	Normal	.00005	.00009	$<0.01^{*a}$
	Tumor	.0002	.0001	

Table 4.2: The statistical results for the PEDXRF system. The same statistical categories displayed in the previous table are presented.
[a] Wilcoxon Signed Ranks test.
* Significance tested at $P < 0.05$

histological analysis and patient history may elaborate on possible causes of this variation. As can be seen in the figures below, elevated levels of previously reported elements in this study are clearly higher in the cancerous tissues. In addition to that, approximately similar trends of box plots for both of the XRF systems are noticeable. However, the normalized counts for copper appears to be higher in the PEDXRF system. It is assumed that this inconsistency in the results of copper may be due to the contamination caused by the materials used to construct the PEDXRF system. Due to the difference in the measurement time between the two XRF systems (30 minutes Vs. 10 minutes), in addition to the increased scatter rejection caused by the PEDXRF system, the inconsistency in counts between systems is expected.

First ROI

Second ROI
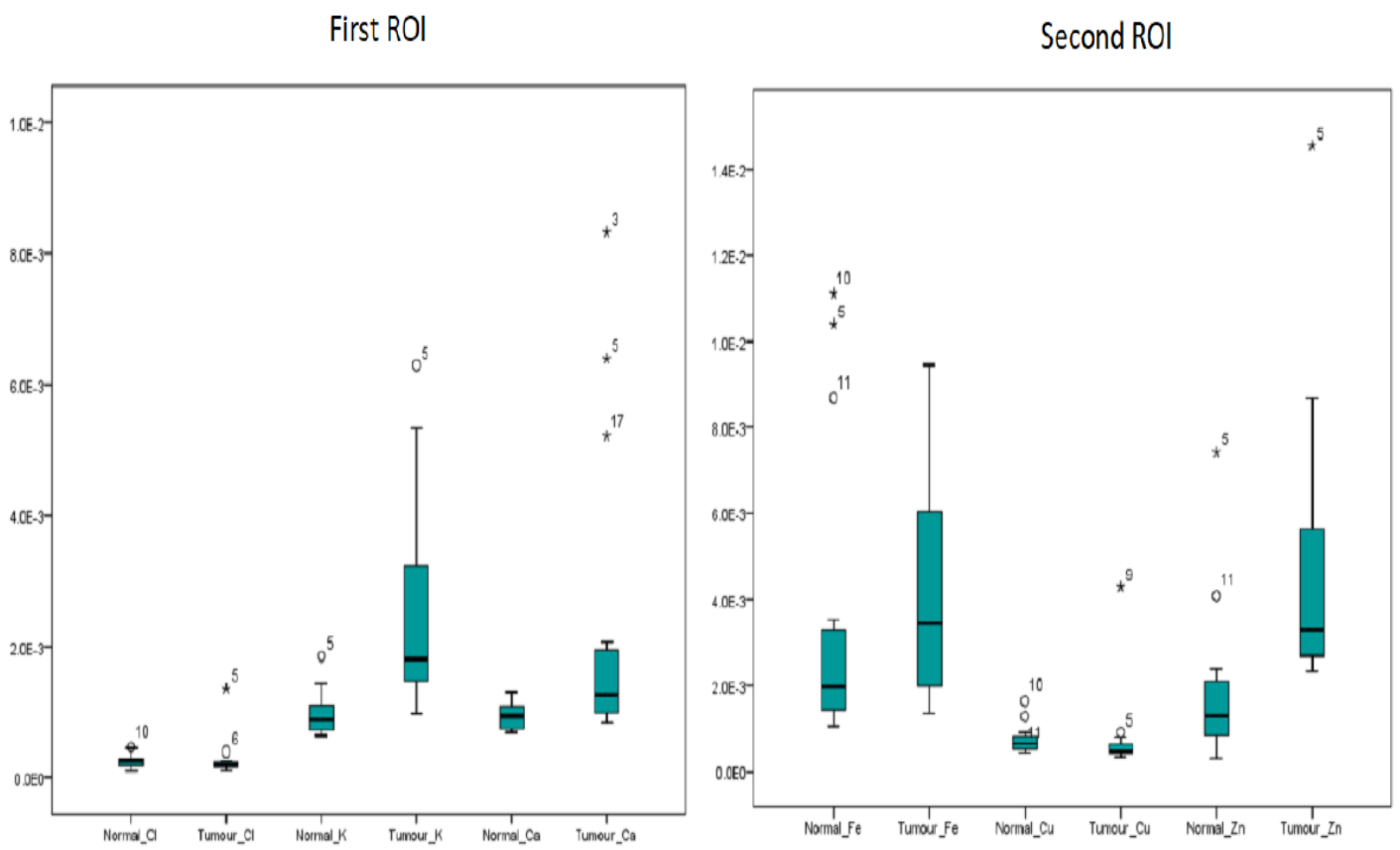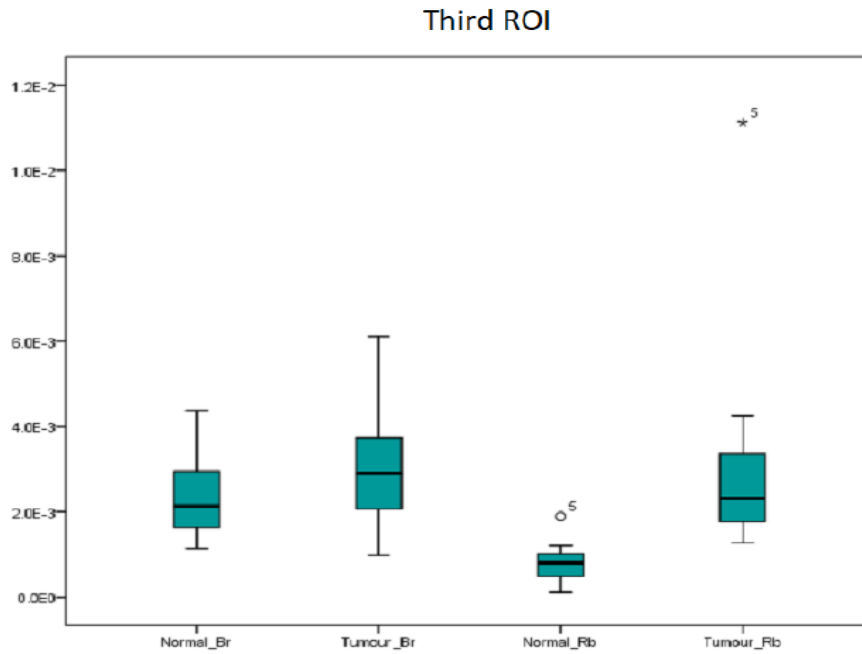
Figure 4.3: Box plots are used to visually present the Huber XRF statistical results, in arbitrary units, of normal and tumor breast tissues for the different elements of interest.
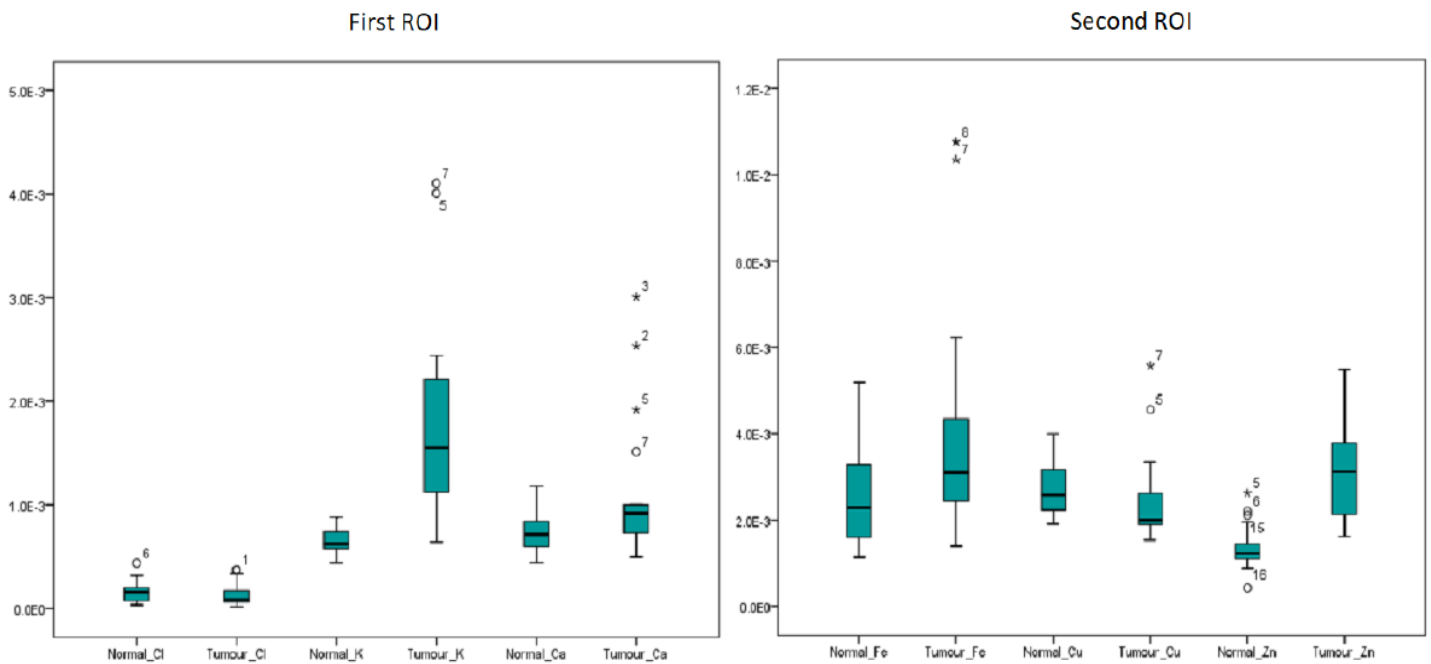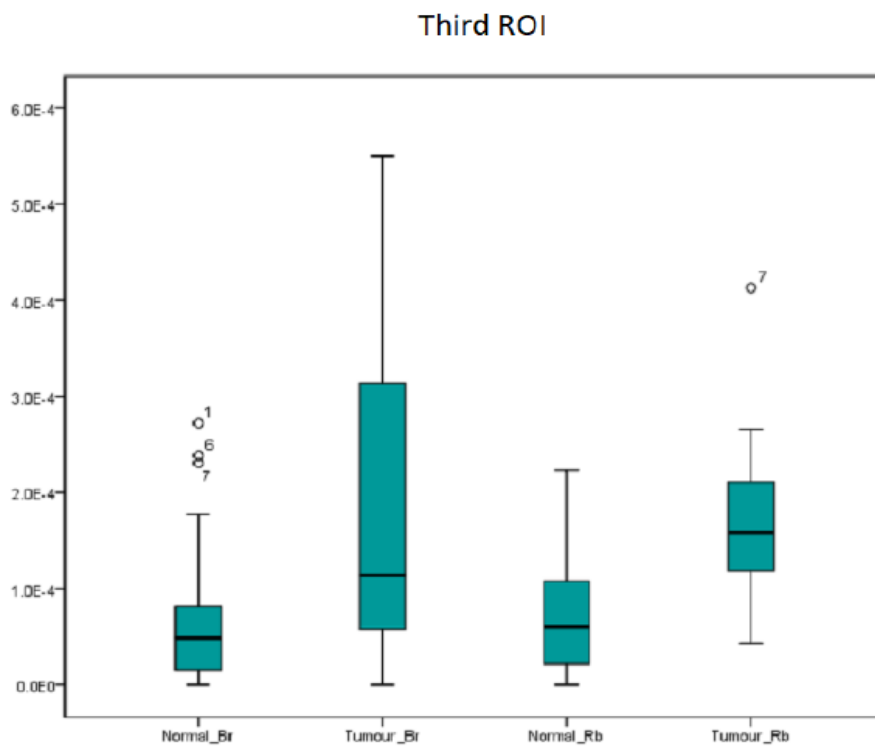
Figure 4.4: Box plots are used to visually present the PEDXRF statistical results. Data is plotted for counts normalized to total scatter versus tissue type and element of interest.

4.1.1   Reproducibility

An essential portion of carrying out a comparison between any two systems performance is to ascertain the accuracy of the reproducibility of measurements. To evaluate the Huber XRF system reproducibility, a single breast specimen was measured. This sample was selected from the same sample set which performed the current experiment. Therefore, no further tissue preparation or procedure was needed for this part of the study. This sample was measured 10 times, each for 30 minutes, consecutively within one day. The X-ray tube was set to $50kV$ and $500\mu A$ similarly to the settings used to acquire the breast tissues data presented earlier. For the PEDXRF system, a lobster hepatopancreas, non-defatted standard reference material (LUTS-1) was used. This reference material is a certified alternative for analyzing trace elements since it possess properties resembling human biological tissues. It should be noted that there is nothing distinctive about the use of two different types of samples to compare the reproducibility of the two systems, but the LUTS-1 material was already utilized to perform a reproducibility study previously using the PEDXRF system separately. The sample was measured on 10 different days with the X-ray tube operated at $50kV$ and $25mA$. Five elements of interest were selected to assess the reproducibility of the two XRF systems. Following the same fitting procedure described in the third chapter, the integral areas of the chosen elements were determined. The obtained integral areas were then normalized to the total scatter to correct for difference in X-ray tube intensities.

Tables 4.3 and 4.4 show the interpretation of statistical results. The uncertainty in the average counts is given by the propagation of error from Poisson statistics and error given from fitting. To test the spread of the data, the standard deviation was

Table 4.3: The Huber XRF reproducibility measurements.

Element	Mean	Std. Error	Std. Deviation	Coefficient of Variation
K	.00446	.00014	.00045	8.9%
Ca	.002097	.000066	.000208	10%
Fe	.00954	.00015	.00046	5.3%
Cu	.000686	.000034	.000109	15.9%
Zn	.00892	.00023	.00072	9.9%

Table 4.4: The PEDXRF reproducibility measurements

Element	Mean	Std. Error	Std. Deviation	Coefficient of Variation
K	.001242	.000051	.000163	12.9%
Ca	.0008036	.0000088	.000163	3.5%
Fe	.002124	.000017	.000052	2.4%
Cu	.007263	.000052	.000165	2.2%
Zn	.004383	.000067	.000211	4.8%

also calculated. The acquired measurements for both of the XRF systems are shown in Figures 4.5 and 4.6. For each XRF system, elements are plotted in two different graphs using multiple colors to help to visualize interfered data. It can be seen from both figures that the Huber XRF and the PEDXRF systems are reproducible and reliable in measuring biological samples. Furthermore, by calculating the relative error of counts corresponded to each element of interest, significantly smaller relative errors are estimated for the Huber XRF system (1%-4%) and the PEDXRF system (6.8E-3%-4%). However, the calculated standard deviations for both of the XRF systems tend to display slightly less spread for the PEDXRF system for two of the measured elements (i.e. Ca and Fe). Overall, it is evident that both of these systems are capable of measuring the elemental compositions for biological specimens precisely.
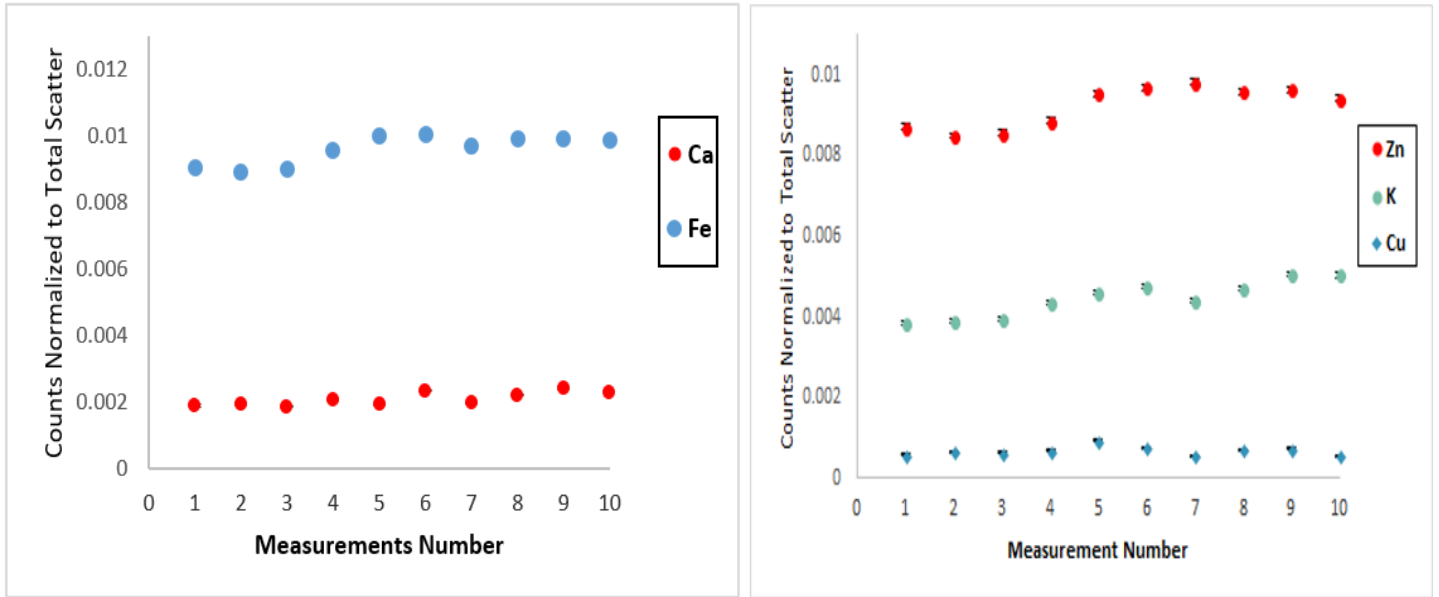
Figure 4.5: The Huber XRF reproducibility measurement for the elements of interest. Error bars are plotted for each element.
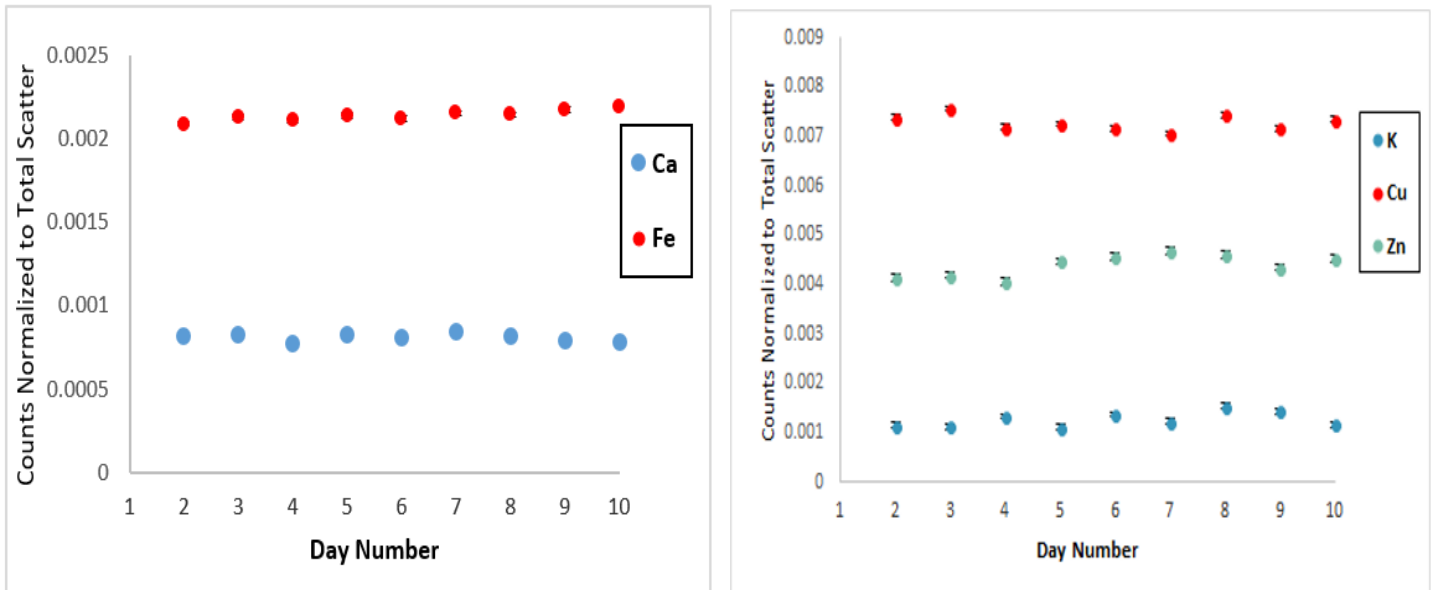
Figure 4.6: The reproducibility measurements for the PEDXRF system are presented. The uncertainty was calculated and plotted for each element.

4.2   X-ray Diffraction Comparison Study

In addition to the important role played by trace elements in vital processes, the difference in the presence of structural components of biological tissues may indicate a morbid condition. XRD techniques have been extensively used to explore the structural differences between normal and tumor breast tissues. It has been evident that incorporating such a powerful technique to the available XRF systems, enhances the extraction of more accurate results when investigating breast specimens. In addition to the importance of obtaining accurate results, acquiring rapid measurements is crucial. For examining the discernible features of normal and malignant breast tissues, ADXRD and EDXRD techniques were introduced to this study. As the second goal of our experiment was to assess the performance of the Huber ADXRD system and the EDXRD technique incorporated to the PEDXRF system, a comprehensive comparison study between the two previously described systems is presented in this section.

4.2.1   Breast Tissues Homogeneity

The first part of the EDXRD study was to examine the homogeneity of the breast specimens for four different sides per sample. Since this technique is capable of providing rapid measurements in a short time (i.e. 10 minutes only), examining the homogeneity of the entire set of the breast specimens was feasible. Observing the obtained data of this part of the study showed no difference between the four sides of each measured sample. Alternatively, the homogeneity between the various edges of each breast specimen was consistent. Two matched-pairs of normal and tumor breast

Tissue	Content	Edge 1	Edge 2	Edge 3	Edge 4	Mean	Std. Error	Std. Deviation
N1	**Adipose**	0.00114	0.00114	0.00120	0.00127	0.00118	0.00003	0.00006
	Fibrous	0.00120	0.00119	0.00116	0.00110	0.00116	0.00002	0.00005
	Water	0.000459	0.000466	0.000450	0.000443	0.000455	0.000005	0.000010
T1	**Adipose**	0.00026	0.00025	0.00022	0.00023	0.00024	0.00001	0.00002
	Fibrous	0.00204	0.00203	0.00206	0.00204	0.00204	0.00001	0.00001
	Water	0.00062	0.00064	0.00064	0.00064	0.00063	0.00001	0.00001
N2	**Adipose**	0.00168	0.00154	0.00172	0.00164	0.00164	0.00004	0.00008
	Fibrous	0.00079	0.00082	0.00077	0.00079	0.00079	0.00001	0.00002
	Water	0.00036	0.00043	0.00036	0.00038	0.00038	0.00002	0.00003
T2	**Adipose**	0.00028	0.00028	0.00026	0.00024	0.00027	0.00001	0.00002
	Fibrous	0.00202	0.00197	0.00200	0.00202	0.00200	0.00001	0.00002
	Water	0.00061	0.00063	0.00063	0.00064	0.00063	0.00001	0.00001

Table 4.5: The content of each edge of the measured samples. The letter "N" represents the normal tissue, while letter "T" indicates the tumor tissue.

tissues were randomly selected to give an example of the homogeneity in the investigated breast tissues. The obtained spectrum for each side of an examined tissue was normalized to unity to account for differences in the X-ray beam intensity. The averaged counts, uncertainty in the mean, and the standard deviation were all calculated and presented in Table 4.5. It is apparent that the different measured edges in the breast tissues are structurally homogeneous. However, the uncertainty associated with fitting and Poisson statistics account for the minor dissimilarity between the calculated contents of each edge for the explored breast samples. Figure 4.7 displays the obtained four spectra for each measured sample. As a result, for the next set of the ADXRD measurements, it was decided that measuring one side of the specimen is adequate. In addition to that, calculating the average of the four sides for each breast sample was chosen to be the best approach to continue the present experiment of the XRD techniques.
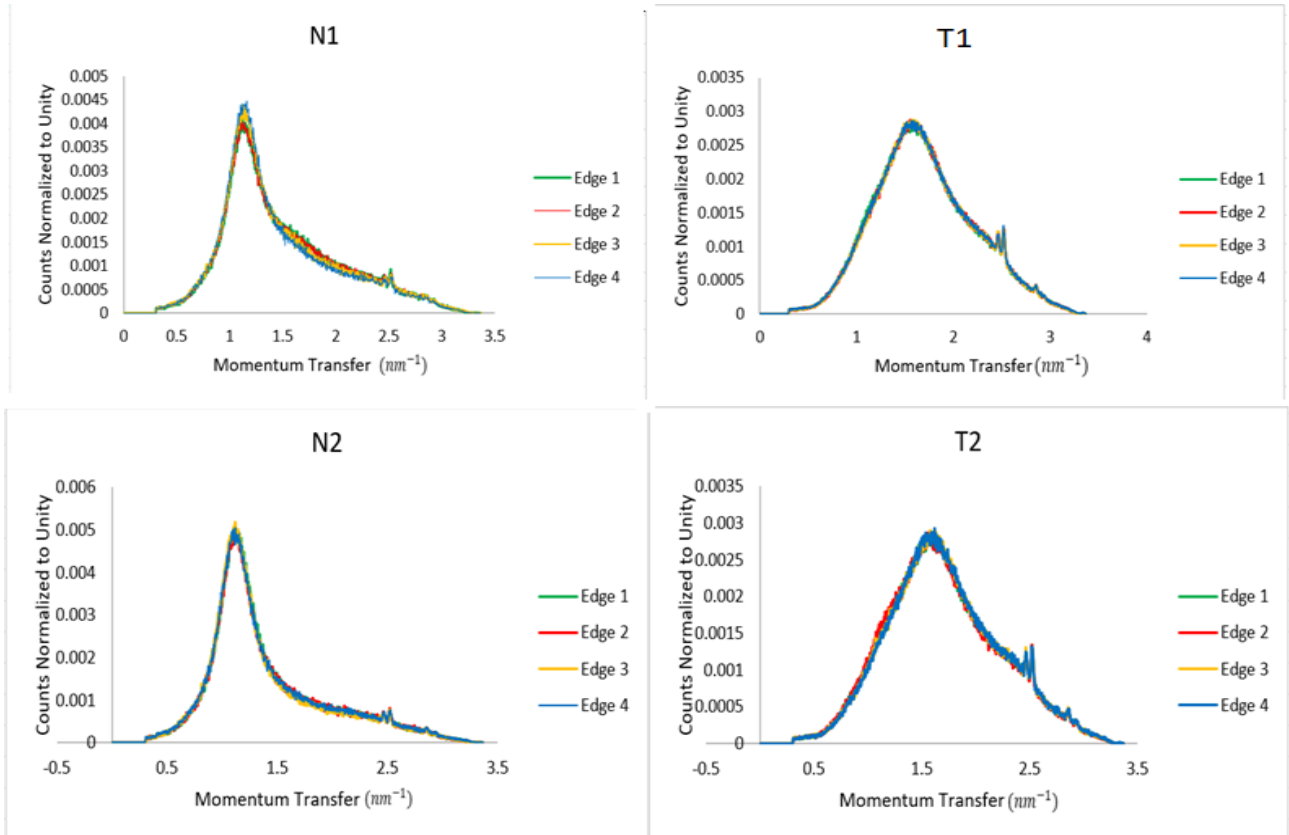
Figure 4.7: The acquired four spectra for each breast sample. Each measured edge displayed with a different color.

4.2.2   Results of EDXRD and ADXRD

The EDXRD technique requires normalizing the X-ray source intensity at different energies with the aim of making results comparable to the ADXRD technique. To accomplish this, first, the output of the X-ray tube has to be obtained. The acquisition of the X-ray tube spectrum was achieved through using Report 78 which is a Spectrum Processor Software. Once the X-ray tube output was obtained, the characteristic X-ray peaks of the tungsten tube were used for calibrating the beam energy. Figure 4.8 illustrates the obtained calibration curve of the utilized X-ray tube. Following tube energy output calibration, plotting the momentum transfer versus counts, as earlier

explained in Chapter 1, was able to be achieved.
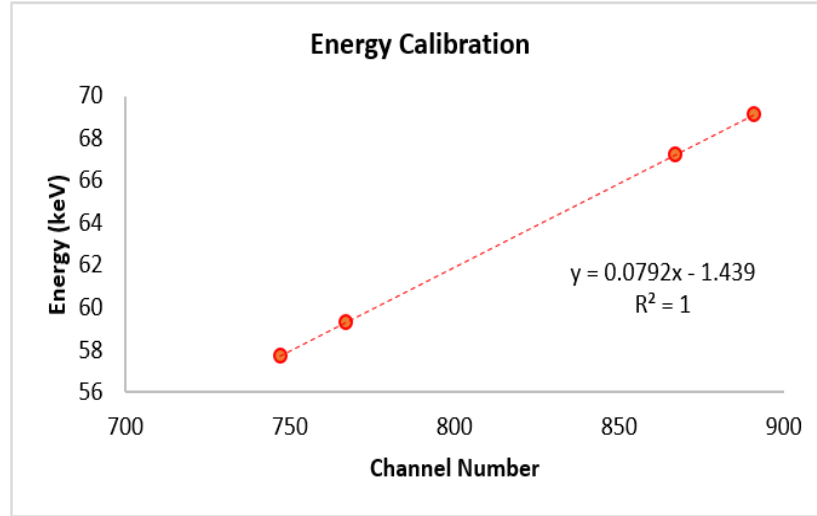
Figure 4.8: The obtained calibration curve to calibrate the X-ray tube energy. A linear regression fit was used to find the correlation between the channel number and the corresponding energy (keV).

For the ADXRD technique, no energy calibration was needed to be able to calculate the momentum transfer, as the angles to be inserted into the momentum transfer equation (present in equation 2.19) were already provided during the experiment. Exploring the coherent scatter profiles associated with the structural components of the breast tissue have demonstrated substantial differences in the composition of the cancerous tissue when compared with the normal tissue. Once again, the data from both systems were normalized to unity first to account for the difference in the X-ray beam intensity and change in time. The results for both of the EDXRD and ADXRD techniques are shown in Tables 4.6 and 4.7 below. To provide a better depiction of the data sets distribution, Figure 4.9 displays the range, median and inter-quartile range (IQR), in arbitrary units, of the contents within breast tissues.

Content	Tissue Type	N	Mean		Std. Deviation	P-Value
			Statistics	Std. Error		
Adipose	Normal	19	0.00083	0.00007	0.00034	$< 0.01^{a*}$
	Tumor	19	0.00032	0.00002	0.00007	
Fibrous	Normal	19	0.00148	0.00006	0.00028	$< 0.01^{b*}$
	Tumor	19	0.00193	0.00002	0.00008	
Water	Normal	19	0.00051	0.00002	0.00008	$< 0.01^{b*}$
	Tumor	19	0.000627	0.000008	0.000032	

Table 4.6: The statistical results obtained for the EDXRD system including the statistical mean, standard error and standard deviation each reported for the healthy and cancerous tissues.
[a] Wilcoxon Signed Ranks test.
[b] Paired-Samples t-test.
* Significance tested at $P < 0.05$

Content	Tissue Type	N	Mean		Std. Deviation	P-Value
			Statistics	Std. Error		
Adipose	Normal	19	0.007	0.001	0.005	$< 0.01^{a*}$
	Tumor	19	0.0012	0.0002	0.0009	
Fibrous	Normal	19	0.008	0.001	0.005	$< 0.01^{b*}$
	Tumor	19	0.0141	0.0007	0.0030	
Water	Normal	19	0.0041	0.0005	0.0022	$< 0.01^{b*}$
	Tumor	19	0.0074	0.0003	0.0015	

Table 4.7: The established statistical results for the ADXRD system. The same statistical categories shown in the previous table are presented.
[a] Wilcoxon Signed Ranks test.
[b] Paired-Samples t-test.
* Significance tested at $P < 0.05$
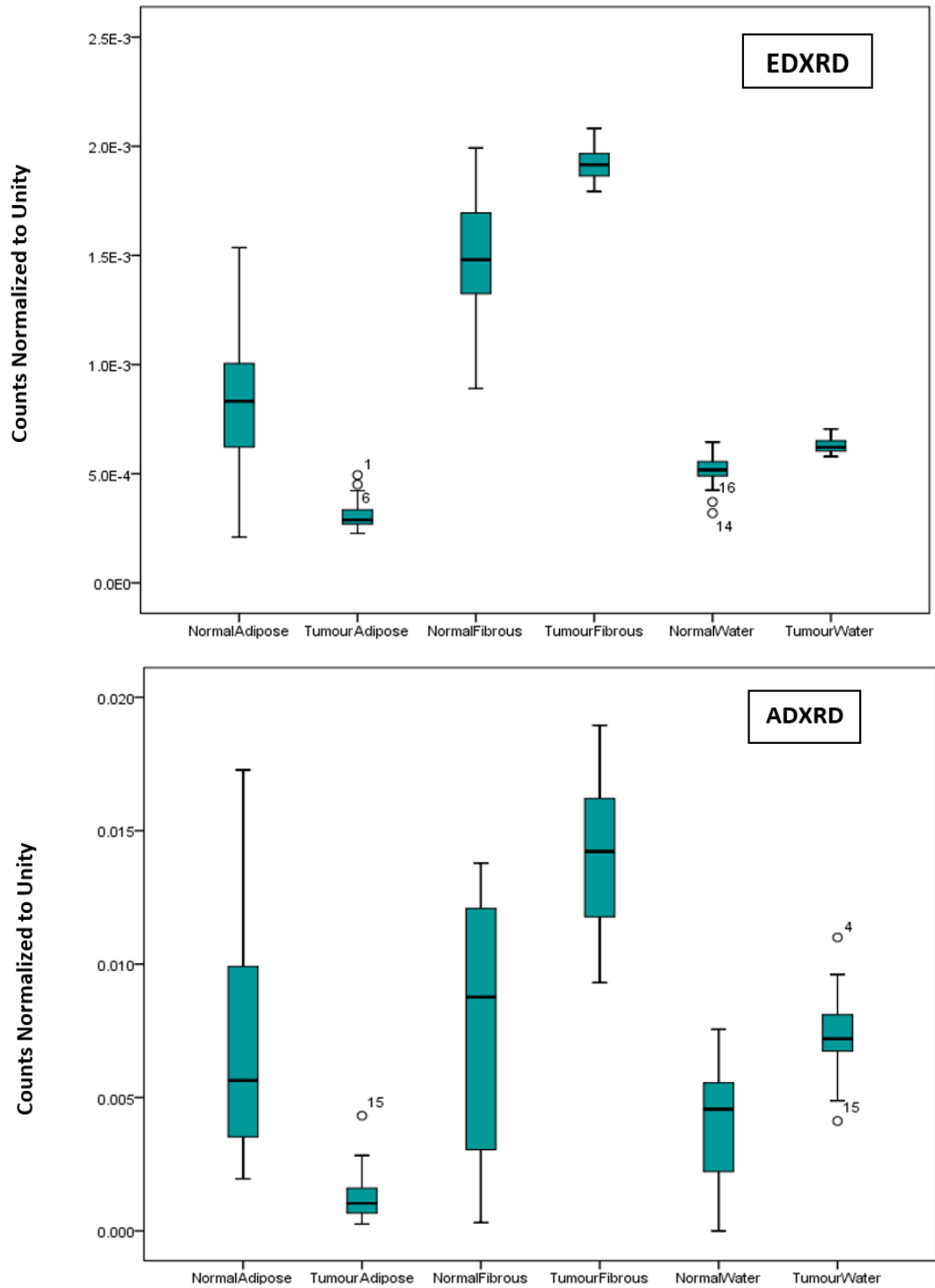
Figure 4.9: Box plots exemplification of the different contents of the examined tumor and normal breast tissues, in arbitrary units, using both of the EDXRD and ADXRD techniques.

From the results achieved by both of the XRD techniques, it can be seen that the adipose content is significantly higher in the normal tissue at $P < 0.01$. While the fibrous and water contents appear to be considerably higher in the tumor specimen at $P < 0.01$ respectively, in a comparison to the healthy tissue. Due to the predominance of the fibrous peak in the cancerous tissue, the increase in the water content was predicted. The obtained XRD statistical results are in a good agreement with the published literature (Geraki *et al.*, 2003; Theodorakou and Farquharson, 2008; Pani *et al.*, 2010).

In order to put the obtained results from both of the EDXRD and ADXRD techniques into perspective, the established data were normalized to the maximum corresponding count to the sample as earlier explained in the methodology chapter. A statistical analysis was conducted to evaluate the two XRD systems. The attained results of the diffraction peaks contents are in a significant agreement to the previously revealed analysis of each system separately. Fortunately, the results established from both XRD approaches have shown to be statistically compatible with each other.

Content	Tissue Type	N	Mean		Std. Deviation	P-Value
			Statistics	Std. Error		
Adipose	Normal	19	0.29	0.01	0.05	$< 0.01^{b*}$
	Tumor	19	0.15	0.01	0.04	
Fibrous	Normal	19	0.42	0.03	0.14	$< 0.01^{a*}$
	Tumor	19	0.615	0.002	0.008	
Water	Normal	19	0.21	0.01	0.06	$< 0.01^{b*}$
	Tumor	19	0.287	0.002	0.007	

Table 4.8: For each measured structural component, the statistical results between normal and tumor breast tissues utilizing the EDXRD approach are presented.
[a] Wilcoxon Signed Ranks test. [b] Paired-Samples t-test.
* Significance tested at $P < 0.05$

Tables 4.8 and 4.9 present the results of the statistical analysis performed on each

Content	Tissue Type	N	Mean		Std. Deviation	P-Value
			Statistics	Std. Error		
Adipose	Normal	19	0.15	0.01	0.06	$< 0.01^{a*}$
	Tumor	19	0.028	0.007	0.033	
Fibrous	Normal	19	0.20	0.03	0.14	$< 0.01^{b*}$
	Tumor	19	0.40	0.02	0.09	
Water	Normal	19	0.10	0.02	0.07	$< 0.01^{b*}$
	Tumor	19	0.19	0.01	0.06	

Table 4.9: The calculated statistical results for the ADXRD system involving the mean, uncertainty in the mean and standard deviation.
[a] Wilcoxon Signed Ranks test.
[b] Paired-Samples t-test.
[*] Significance tested at $P < 0.05$

XRD technique. It can be seen from the tables that the contents of each tissue measured in the EDXRD and ADXRD is remarkably equivalent. For instance, as shown in Table 4.8, the difference in the normalized mean for the adipose content between the normal and tumor tissue being measured on the EDXRD system is approximately 0.14. By observing the ADXRD results given in Table 4.9, the statistical difference between the healthy and tumor specimens corresponds to roughly 0.13, making it analogous to that found by the EDXRD technique. Similar trends of the analyzed diffraction peaks obtained by both of the EDXRD and ADXRD systems are observed. In addition, the other calculated statistical values such as the standard error and standard deviation are observed to be approximately similar between the two systems. As a consequence of these results, it is evident that both of the XRD approaches are capable of statistically providing similar results for the observed diffraction profiles of the interrogated breast specimens. Figure 4.10 presents the averaged counts of normal and tumor tissues for EDXRD and ADXRD techniques. Similar trends of the tissue contents are noticeable between the two XRD methods.
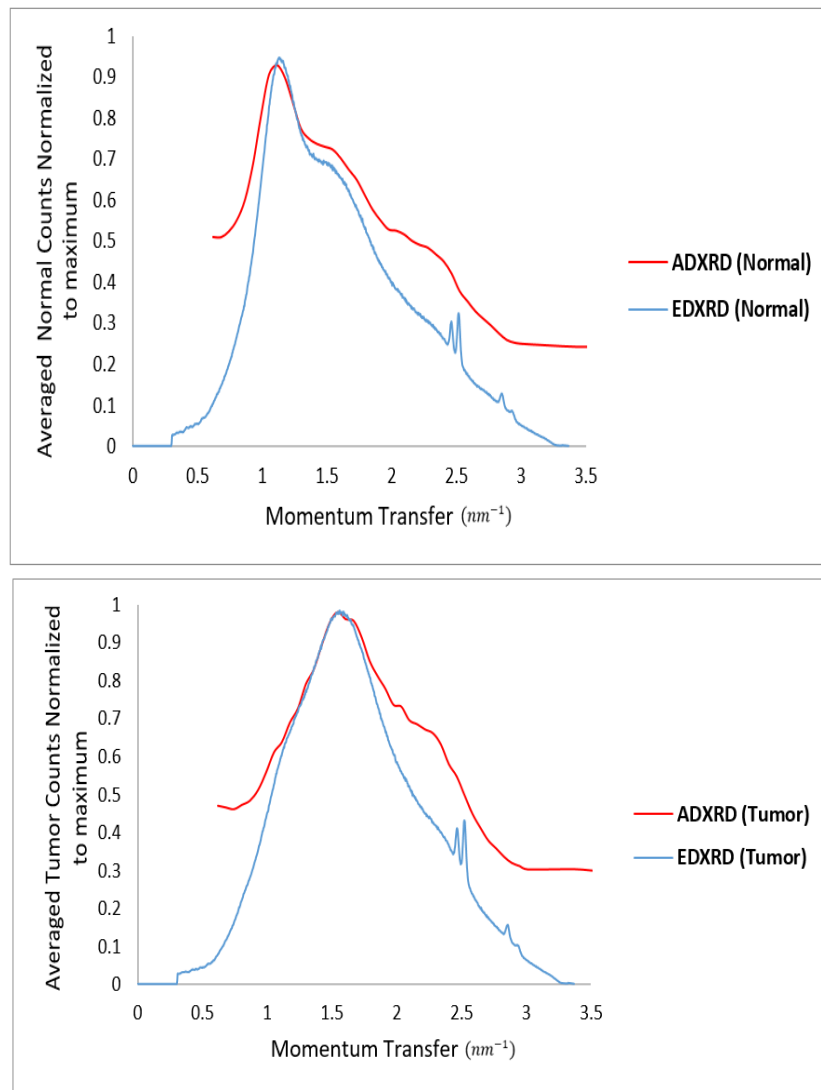
Figure 4.10: The averaged counts of normal and tumor tissues for the EDXRD and ADXRD techniques prior to the background subtraction.

4.2.3   Reproducibility

To accomplish the goal of investigating the features and differences between each XRD spectrometers incorporated in both earlier mentioned X-ray detection systems, breast cancerous specimens were selected to assess the reproducibility of these systems. While both tumor and healthy breast tissues possess dissimilar structural components, choosing the tumor samples in this experiment was decided due to their predicted large content of fibrous structures, which can be used to test reproducibility. Examining the reproducibility of the EDXRD system was already performed on a different breast sample, therefore, the previously acquired measurements were re-used and combined with the current study. The two breast samples were then measured separately and repeatedly ten times using both the EDXRD and ADXRD techniques. The X-ray tube for the EDXRD experiment was operated at $80kV$ and $8mA$ with the sample being measured for 10 minutes only. Whereas, for the ADXRD reproducibility measurements, the sample was measured for 60 minutes with the X-ray tube set to $50kV$ and $500\mu A$. By applying the fitting procedure explained in Chapter 3, the integral area of each diffraction peak of interest (i.e. adipose, fibrous and water) was obtained. The achieved reproducibility results of each XRD modality were ultimately statistically analyzed.

Following the error propagation calculation from Poisson statistics, error given from fitting and standard deviation calculation, the statistical results for the reproducibility of both ADXRD and EDXRD systems were attained. The obtained statistical results are displayed in Tables 4.10 and 4.11. The reproducibility in measurements for both systems are represented in Figure 4.11.

From observing Tables 4.10, 4.11 and the plots given in Figure 4.10, it is apparent

Content	Mean	Std. Error	Std. Deviation	Coefficient of Variation
Adipose	.0004192	.0000040	.0000127	3.10%
Fibrous	.0019775	.0000028	.0000087	.455%
Water	.00061718	.00000053	.00000168	.275%

Table 4.10: The statistical results for the reproducibility of the EDXRD technique.

Content	Mean	Std. Error	Std. Deviation	Coefficient of Variation
Adipose	.00243	.00029	.00093	37.6%
Fibrous	.01460	.00020	.00064	4.11%
Water	.00606	.00017	.00055	8.20%

Table 4.11: The obtained statistical results for the reproducibility of the ADXRD technique.

that the EDXRD system has superior reproducibility in measurements in comparison to the ADXRD system. n, examining the reproducibility of each system was conducted using two different breast specimens, as a result, the contents of each tissue was predicted to be different. However, by looking at the results given in Tables 4.10 and 4.11, it is clear that the standard error values of the averaged counts of the tissue contents are significantly lower for the EDXRD system. Similarly, the standard deviation values calculated for the tissue components indicate less spread in the distribution of the EDXRD data. Furthermore, by calculating the relative error, it is established that the relative error varies between roughly 0.08% and 0.95% with the EDXRD system. Whereas for the ADXRD system, the relative error varies between approximately 1.4% and 12.04%. The superiority in the achieved statistical results of the EDXRD system was not surprising. Since the EDXRD system utilizes a polychromatic source with a great photon flux.
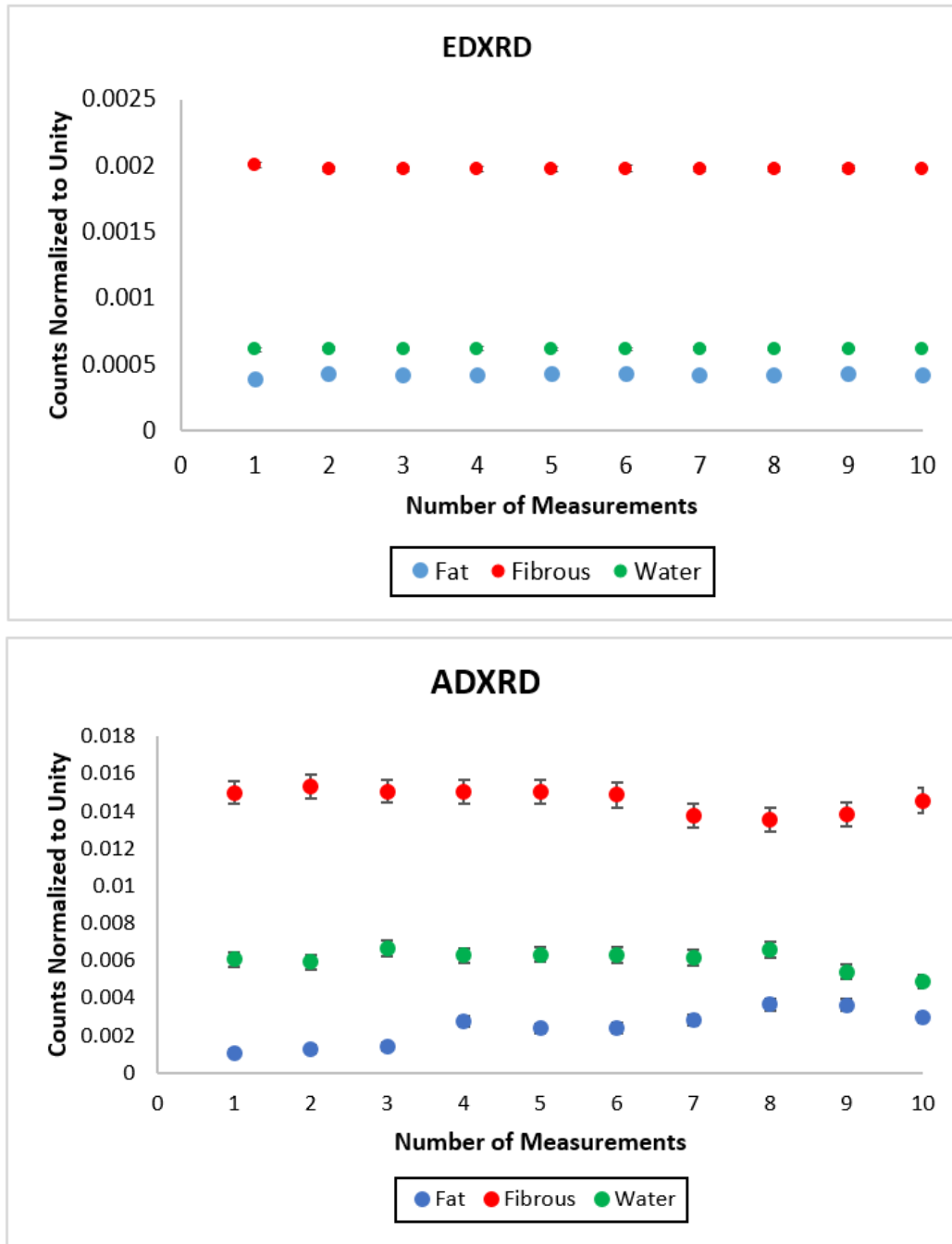
Figure 4.11: The acquired EDXRD and ADXRD reproducibility measurements of different tissue contents. Each content is plotted in different color to aid in visualization.

Chapter 5

Conclusion and Future Work

For the past several decades, efforts have been dedicated to developing techniques that aid in understanding the mechanism behind breast cancer and the way it develops, in order to expedite diagnosis and treatment of disease. Some of these techniques are based on the assumption that the concentration of trace elements varies in a cancerous tissue when compared with healthy tissue, in addition to the variation in the structural homogeneity of the examined samples. This pilot study was conducted in order to assess the performance of two dissimilar X-ray detection systems; a conventional monochromatic X-ray system for X-ray Fluorescence (XRF) and Angular Dispersive X-ray Diffraction (ADXRD) techniques, and a combined Polarized Energy Dispersive X-ray Fluorescence (PEDXRF) and Energy Dispersive X-ray Diffraction (EDXRD) system. While each of the aforementioned detection systems possesses distinctive characteristics, a biological set constituting 19 matched-pairs of healthy and cancerous breast specimens was used to implement a comprehensive comparison study between the two systems. A primary study involved evaluating and investigating the different XRF techniques of each system was conducted. Achieving this goal

was feasible through the quantification of the following trace elements: Cl, K, Ca, Fe, Cu, Zn, Br and Rb. Focusing the attention on these elements in particular was due to their prominent roles of differentiating between a tumor and normal breast tissues, which can be used as robust biomarkers to indicate a morbid condition (Silva *et al.*, 2009). The second objective of the present study was to highlight the features and discrepancies between each XRD spectrometer incorporated in both systems by examining the structural components (i.e. adipose, fibrous and water) of the same breast tissues. A number of studies have sought to elucidate the variation in the shape and contents of structural components of both healthy and cancerous breast tissues (Geraki *et al.*, 2003; Ryan and Farquharson, 2007). Furthermore, these studies have demonstrated that a sharp adipose peak emerges in the healthy tissue at a momentum transfer corresponds to $1.1nm^{-1}$, while for the malignant tissue, a sharp fibrous peak is revealed at $1.6nm^{-1}$. Overall, it is strongly believed that incorporating such powerful techniques as XRF and XRD in an individual clinical detection system, enhances the ability to obtain more accurate results for the purpose of diagnosing investigated specimens.Conclusions of the present study, in addition to a discussion of the different aspects and results achieved from both aforementioned systems, are illustrated below.

5.1   XRF Study

Two different types of the XRF techniques were compared in this study through the measurement of trace elements in breast specimens. The first XRF technique was based on utilizing a conventional monochromatic X-ray beam up to 17.44 keV and focused to deliver a $1.8 \times 1.8mm^2$ beam area of approximately 3.5×10^6 photons per

second on the sample. With this sytem, each breast sample was measured for 30 minutes. The source of the X-rays in the conventional system was a molybdenum target, that was fully integrated within the system. The next XRF instrumentation was the PEDXRF tool, which was dependent on a strict geometry involving several collimators and placing the experiment equipment in a Cartesian set-up. Achieving this configuration is mandatory to not only produce a polarized beam towards the sample, but also to attain a dramatic reduction in the scatter. A polychromatic source was used accompanied by a powerful X-ray tube, which has the advantage of producing more characteristic X-rays and reducing the measurements acquisition time. In addition to the two previous requirements, a suitable secondary target must be used. The PEDXRF system, depending on the goal of the experiment, offers a great advantage of using three different types of metallic secondary targets, molybdenum, copper and zinc. For the current study, a molybdenum metallic target was used to excite elements within the range of interest. The size of the beam produced from the PEDXRF system corresponds to an elliptical shape ($10mm$ and $15mm$ in the semi-minor and semi-major axis respectively) covering approximately all of the measured specimen. Acquiring the dataset of investigated specimens was accomplished in a time intervals of 10 minutes per sample.

A number of various characteristics can be observed between the Huber XRF system and the PEDXRF system. The first notable feature is the ability of the PEDXRF system to suppress scattered X-rays towards the sample. As a result, a significant improvement in the minimum detection limits and signal-to-noise ratio (SNR) are achievable (Johnston, 2017), which thereby aids in attaining more accurate information on the examined specimen. Secondly, the beam size of the Huber XRF system is

remarkably smaller when compared to the PEDXRF system. Furtheromre, the Huber XRF beam spot size covers approximatley $1.8 \times 1.8 mm^2$ of a sample, while for the PEDXRF system, an elliptical spot size covers most of the sample. A larger beam size would allow for measuring large samples in the future, with the option to collimate the beam in the case of smaller sample sizes since the ideal beam size matches that of the sample dimensions. For clarification, if the case was a small size sample to be measured using the Huber XRF system, as the beam size for this system is quite small, if the beam did not strike the sample, a failure in the measurement is predicted. Therefore, prior to initiating any measurements on the Huber XRF spectrometer, a radiochromic film is normally utilized to ensure the path of the X-rays will interact with a sample. Another distinguished advantage of the PEDXRF system, is the ability to employ various types of secondary targets to perform different experiments that depend on exciting a unique element, or multiple elements within a different range of energies. While the Huber XRF system is limited to only exciting elements with absorption edges close to its molybdenum X-ray target's energy, the PEDXRF has interchangeable targets. Assessing both XRF systems also reveals another feature of the PEDXRF system, which is the capability of acquiring measurements of an investigated biological sample within 10 minutes only in comparison to the Huber XRF system which requires at least 30 minutes.

Evaluating the concentrations of the examined trace elements by employing the different XRF techniques have revealed a statistically significant increase in the levels of K, Ca, Fe, Zn and Rb in the cancerous tissue in contrast to the healthy tissue at $P < 0.01$. These results are in line with the findings of Farquharson [3]; nevertheless, the obtained results of Cl, Cu and Br have indicated insignificant difference between

the normal and tumor specimens. The results obtained from both of the Huber XRF and PEDXRF techniques have demonstrated statistically consistent results for both detection systems. Although the PEDXRF system has tremendous features, due to the impurities in the materials utilized to construct the system, inaccuracy in the amount of the copper in an examined sample would result. In addition to that, owing to the collimators required to implement the polarized-EDXRF experiment, L-level characteristic X-rays of lead are detected. However, it was shown that these L characteristic X-rays did not interfere with any of the measured elements in the presented study. From another perspective, since it was able to detect these high atomic number characteristic X-rays, this system has shown significant sensitivity for investigating elements with higher atomic numbers. An important aspect to investigate in both XRF systems was the reproducibility of measurements. Both of the Huber XRF and the PEDXRF spectrometers have statistically shown great reproducibility in measuring breast specimens. Although it is true that both of these systems have demonstrated their ability to precisely measure biological specimens, the PEDXRF system possesses a great advantage of acquiring data in rapid time.

5.2   XRD study

The same abovementioned breast specimens were used to assess the performance of the EDXRD and ADXRD spectrometers. The EDXRD experiment is based on utilizing a collimated beam matching the sample holder size and a polychromatic source, which aids in producing a high beam flux and a rapid measurement time. The data were collected in 10 minutes, with the sample holder placed on an aluminum block and diffracted at 6° angle. It is worth noting that this block constitutes multiple

angles ranging from $3^o - 13^o$ to perform different experiments at any desired angle(s) in the given diffraction range. For the ADXRD spectrometer, since this technique is incorporated into the conventional monochromatic system, and hence utilizes a fixed energy, it required at least 60 minutes per sample to obtain data in this experiment. As earlier mentioned in the XRF study discussion part, since the beam size corresponds to a $1.8 \times 1.8mm^2$ square spot, to ensure the beam path travels towards a sample prior to irradiating, radiochromic film was used. Each breast sample in this experiment was measured within a range of angles corresponds to $5^o - 52^o$. While the EDXRD system requires calibrating the source energy, there is no need for that with the ADXRD system.

Since the EDXRD spectrometer is capable of measuring samples within a significantly short time, a study to examine the homogeneity of the breast tissues was conducted. This experiment has shown a statistically prominent homogeneity in the breast samples. Following this investigation, an analysis of the structural diffraction patterns of the samples was conducted. The obtained results using both of the XRD modalities have revealed a statistically strong agreement with the previous literature. The results established from both XRD approaches have shown to be statistically compatible with each other. An interrogation of the reproducibility of measurements was also performed for both of the EDXRD and ADXRD systems. The acquired data have demonstrated more consistent results for the EDXRD technique.

5.3   Future Work

In conclusion, this project has proven that both the Huber monochromatic X-ray system for XRF and ADXRD techniques, and the combined PEDXRF and EDXRD

system, have shown favourable results for the interrogated breast specimens. However, the combined PEDXRF and EDXRD system has revealed an increase in the performance when compared to the traditional Huber X-rays system. Although this is true, a number of suggestions are made to improve the combined PEDXRF and EDXRD system performance and effectiveness, and enhance the results of the comparison study between the two X-rays systems. First, since the fundamental objective of these systems is to classify biological specimens, a larger set of different types of biological specimens should be investegated. Furthermore, enlarging the sample size would improve the statistical results and aid in assessing the accuracy in results acquired from the utilized two systems for discriminating biological samples. Similarly, investigating other types of biological specimens such as liver or lung or any other available specimens with the purpose of comparing the obtained results, could assist in exploring the employed X-ray systems functionality and features for different structures and elemental compositions than that of breast tissues. Another suggestion for future work, sample model classifications such as Principal Component Analysis (PCA) and Multiple Correspondence Analysis (MCA) are encouraged to be used to recognize patterns in data sets as well as discriminate between different properties of unkown specimens. This has a positive impact on validating the obtained results from interrogated biological samples.

As earlier mentioned, the combined PEDXRF and EDXRD spectrometer has shown tremendous ability for differentiating tumor and normal breast samples. Nevertheless, some particular aspects are proposed to be improved. Furthermore, since it is believed that copper is deposited in the materials constructed this system, which thereby causes inaccuracy in results, eliminating this issue should be addressed. In

addition, while the lead L characteristic X-rays did not overlap with any measured elements in this work, to avoid any future intervention with spectra acquisition, manufacturing the collimators from other materials than lead is suggested. Besides these two elements, a common XRF signal arising from nickel was noticeable in both of the Huber XRF and the combined PEDXRF systems. Although the nickel signal did not interfere with any of the measured elements, considerations should be made to remove it from spectra of biological samples under investigation.

Overall, as the objective of this study was to assess two different X-ray detection systems, both of these systems have proven their proficiency for differentiating normal and tumor breast specimens. In spite of this, the combined PEDXRF and EDXRD system has shown promising results in comparison to the conventional X-ray system. Possessing higher flux, acquiring rapid measurements, and the choice of utilizing different type of secondary targets for XRF studies, all account for the superiority of this system. It is true that this X-ray detection system is still under improvement, but it's robustness and rapidity indicate a significant advancement in this field.

Bibliography

Abuhani, W. A., Dasgupta-Schubert, N., and Cendejas, L. M. V. (2014). Character-
izing fundamental parameter-based analysis for soil–ceramic matrices in polarized
energy-dispersive x-ray fluorescence (pedxrf) spectrometry. *Powder Diffraction*,
29(2), 159–169.

Al-Bahri, J. S. and Spyrou, N. M. (1998). Electron density of normal and pathological
breast tissues using a compton scattering technique. *Applied radiation and isotopes*,
49(12), 1677–1684.

Al-Ebraheem, A., Farquharson, M. J., and Ryan, E. (2009). The evaluation of biolog-
ically important trace metals in liver, kidney and breast tissue. *Applied Radiation
and Isotopes*, **67**(3), 470–474.

Als-Nielsen J., M. D. (2001). *Elements of Modern X-Ray Physics.pdf*.

Alvarez, R. P., Markowicz, A., Wegrzynek, D., Cano, E. C., Bamford, S., and Torres,
D. H. (2007). Quality management and method validation in edxrf analysis. *X-Ray
Spectrometry*, **36**(1), 27–34.

BEARDEN, J. A. (1967). X-ray wavelengths. *Rev. Mod. Phys.*, **39**, 78–124.

Beckhoff, B., Kanngiesser, B., Langhoff, N., Wedell, R., and Wolff, H. (2006). *Handbook of Practical X-Ray Fluorescence Analysis.* Springer Berlin Heidelberg, Berlin, Heidelberg.

Bushberg, J. T., Seibert, J. A., Leidholdt, E. M., Boone, J. M., and Goldschmidt, E. J. (2003). The essential physics of medical imaging. *Medical Physics*, **30**(7), 1936–1936.

Chaparian, A., Oghabian, M., Changizi, V., and Farquharson, M. (2010). The optimization of an energy-dispersive x-ray diffraction system for potential clinical application. *Applied Radiation and Isotopes*, **68**(12), 2237–2245.

Conceição, A., Antoniassi, M., Poletti, M., and Caldas, L. (2010). Preliminary study of human breast tissue using synchrotron radiation combining waxs and saxs techniques. *Applied Radiation and Isotopes*, **68**(4), 799–803.

Costello, L. and Franklin, R. (1998). Novel role of zinc in the regulation of prostate citrate metabolism and its implications in prostate cancer. *The Prostate*, **35**(4), 285–296.

Cui, Y., Vogt, S., Olson, N., Glass, A. G., and Rohan, T. E. (2007). Levels of zinc, selenium, calcium, and iron in benign breast tissue and risk of subsequent breast cancer. *Cancer Epidemiology and Prevention Biomarkers*, **16**(8), 1682–1685.

Curry, T. S., Dowdey, J. E., Murry, R. C., and Christensen, E. E. (1990). *Christensen's physics of diagnostic radiology.* Lea & Febiger.

de Vega, R. G., Fernández-Sánchez, M. L., Pisonero, J., Eiró, N., Vizoso, F. J., and

Sanz-Medel, A. (2017). Quantitative bioimaging of ca, fe, cu and zn in breast cancer tissues by la-icp-ms. *Journal of Analytical Atomic Spectrometry*, **32**(3), 671–677.

Elshemey, W. M., Elsayed, A. A., and El-Lakkani, A. (1999). Characteristics of low-angle x-ray scattering from some biological samples. *Physics in medicine and biology*, **44**(12), 2907.

Evans, S., Bradley, D., Dance, D., Bateman, J., and Jones, C. (1991). Measurement of small-angle photon scattering for some breast tissues and tissue substitute materials. *Physics in medicine and biology*, **36**(1), 7.

Farquharson, M., Al-Ebraheem, A., Falkenberg, G., Leek, R., Harris, A., and Bradley, D. (2008). The distribution of trace elements ca, fe, cu and zn and the determination of copper oxidation state in breast tumour tissue using μsrxrf and μxanes. *Physics in medicine and biology*, **53**(11), 3023.

Farquharson, M., Al-Ebraheem, A., Cornacchi, S., Gohla, G., and Lovrics, P. (2013). The use of x-ray interaction data to differentiate malignant from normal breast tissue at surgical margins and biopsy analysis. *X-Ray Spectrometry*, **42**(5), 349–358.

Farquharson, M. J. and Geraki, K. (2004). The use of combined trace element XRF and EDXRD data as a histopathology tool using a multivariate analysis approach in characterizing breast tissue. *X-Ray Spectrometry*, **33**(4), 240–245.

Garg, A., Singh, V., Weginwar, R., and Sagdeo, V. (1994). An elemental correlation study in cancerous and normal breast tissue with successive clinical stages by neutron activation analysis. *Biological Trace Element Research*, **46**(3), 185–202.

Geraki, K. and Farquharson, M. (2001). An x-ray fluorescence system for measuring trace element concentrations in breast tissue. *Radiation physics and chemistry*, **61**(3), 603–605.

Geraki, K., Farquharson, M., and Bradley, D. (2003). X-ray fluorescence and energy dispersive x-ray diffraction for the quantification of elemental concentrations in breast tissue. *Physics in medicine and biology*, **49**(1), 99.

Griffiths, J., Royle, G., Hanby, A., Horrocks, J., Bohndiek, S., and Speller, R. (2007). Correlation of energy dispersive diffraction signatures and microct of small breast tissue samples with pathological analysis. *Physics in medicine and biology*, **52**(20), 6151.

Griffiths, J., Royle, G., Horrocks, J., Hanby, A., Pani, S., and Speller, R. (2008). Angular dispersive diffraction microct of small breast tissue samples. *Radiation Physics and Chemistry*, **77**(4), 373–380.

Harding, G., Kosanetzky, J., and Neitzel, U. (1987). X-ray diffraction computed tomography. *Medical physics*, **14**(4), 515–525.

Heckel, J., Brumme, M., Weinert, A., and Irmer, K. (1991). Multi-element trace analysis of rocks and soils by edxrf using polarized radiation. *X-Ray Spectrometry*, **20**(6), 287–292.

Heckel, J., Haschke, M., Brumme, M., and Schindler, R. (1992). Principles and applications of energy-dispersive x-ray fluorescence analysis with polarized radiation. *Journal of analytical atomic Spectrometry*, **7**(2), 281–286.

Johnston, E. (2017). *Design, Optimization, and Testing of a Combined Tri-Axial Polarized Energy Dispersive X-Ray Fluorescence and Energy Dispersive X-Ray Diffraction System for Biological Sample Classification*. Ph.D. thesis.

Johnston, E. M., Byun, S. H., and Farquharson, M. J. (2017). Determination of optimal metallic secondary target thickness, collimation, and exposure parameters for X-ray tube-based polarized EDXRF. *X-Ray Spectrometry*, **46**(2), 93–101.

Kidane, G., Speller, R., Royle, G., and Hanby, A. (1999). X-ray scatter signatures for normal and neoplastic breast tissues. *Physics in Medicine and Biology*, **44**(7), 1791.

Knoll, G. F. (2000). *Radiation Detection and Measurement*, volume 3.

Kosanetzky, J., Knoerr, B., Harding, G., and Neitzel, U. (1987). X-ray diffraction measurements of some plastic materials and body tissues. *Medical physics*, **14**(4), 526–532.

Lappano, R., Malaguarnera, R., Belfiore, A., and Maggiolini, M. (2017). Recent advances on the stimulatory effects of metals in breast cancer. *Molecular and cellular endocrinology*, **457**, 49–56.

LeClair, R. J., Boileau, M. M., and Wang, Y. (2006). A semianalytic model to extract differential linear scattering coefficients of breast tissue from energy dispersive x-ray diffraction measurements. *Medical physics*, **33**(4), 959–967.

Lewis, R. A., Rogers, K., Hall, C. J., Towns-Andrews, E., Slawson, S., Evans, A., Pinder, S., Ellis, I., Boggis, C., Hufton, A. P., *et al.* (2000). Breast cancer diagnosis using scattered x-rays. *Journal of synchrotron radiation*, **7**(5), 348–352.

Liqiang, R. (2016). X-ray spectral analysis in x-ray fluorescence imaging for breast cancer detection.

Majewska, U., Banaś, D., Braziewicz, J., Góźdź, S., Kubala-Kukuś, A., and Kucharzewski, M. (2007). Trace element concentration distributions in breast, lung and colon tissues. *Physics in medicine and biology*, **52**(13), 3895.

Marguí, E., Padilla, R., Hidalgo, M., Queralt, I., and Van Grieken, R. (2006). High-energy polarized-beam edxrf for trace metal analysis of vegetation samples in environmental studies. *X-Ray Spectrometry*, **35**(3), 169–177.

Markowicz, a., Wegrzynek, D., Chinea-Cano, E., Bamford, S. a., Torres, D. H., and Alvarez, R. P. (2007). Quality management and method Validation in EDXRF analysis. *X-Ray Spectrometry*, **36**(1), 27–34.

Marticke, F. (2016a). Optimization of an X-ray diffraction imaging system for medical and security applications.

Marticke, F. (2016b). Optimization of an X-ray diffraction imaging system for medical and security applications.

Marticke, F., Montémont, G., Paulus, C., Mars, J., Michel, O., and Verger, L. (2015). Energy dispersive x-ray diffraction system as a promising virtual biopsy in mammography. In *2015 IEEE Nuclear Science Symposium and Medical Imaging Conference.*

Marticke, F., Montémont, G., Paulus, C., Michel, O., Mars, J., and Verger, L. (2017). Simulation study of an x-ray diffraction system for breast tumordetection. *Nuclear*

Instruments and Methods in Physics Research Section A: Accelerators, Spectrometers, Detectors and Associated Equipment, **867**, 20–31.

McLaughlin, J. and Schuman, L. (1983). Epidemiology of renal cell carcinoma. *Reviews in cancer epidemiology*, **2**, 170–210.

Moss, R., Crews, C., Wilson, M., and Speller, R. (2017). minipixd: a compact sample analysis system which combines x-ray imaging and diffraction. *Journal of Instrumentation*, **12**(02), P02001.

Narten, A. and Levy, H. (1971). Liquid water: Molecular correlation functions from x-ray diffraction. *The Journal of Chemical Physics*, **55**(5), 2263–2269.

Ng, K., Bradley, D., and Looi, L. (1997). Elevated trace element concentrations in malignant breast tissues. *The British journal of radiology*, **70**(832), 375–382.

O'Flynn, D., Reid, C., Christodoulou, C., Wilson, M., Veale, M., Seller, P., Hills, D., Desai, H., Wong, B., and Speller, R. (2013). Explosive detection using pixellated x-ray diffraction (pixd). *Journal of Instrumentation*, **8**(03), P03007.

OFlynn, D., Desai, H., Reid, C. B., Christodoulou, C., Wilson, M. D., Veale, M. C., Seller, P., Hills, D., Wong, B., and Speller, R. D. (2013). Identification of simulants for explosives using pixellated x-ray diffraction. *Crime Science*, **2**(1), 4.

Pani, S., Cook, E., Horrocks, J., Jones, J., and Speller, R. (2010). Characterization of breast tissue using energy-dispersive x-ray diffraction computed tomography. *Applied Radiation and Isotopes*, **68**(10), 1980–1987.

Parkin, D. M., Bray, F., and Devesa, S. (2001). Cancer burden in the year 2000. the global picture. *European journal of cancer*, **37**, 4–66.

Poletti, M., Gonçalves, O., and Mazzaro, I. (2002). Coherent and incoherent scattering of 17.44 and 6.93 kev x-ray photons scattered from biological and biological-equivalent samples: characterization of tissues. *X-Ray Spectrometry*, **31**(1), 57–61.

Post, B. (1999). X-Ray Characterization of Materials. *Wiley*, pages 1–103.

Raju, G. N., Sarita, P., Kumar, M. R., Murty, G. R., Reddy, B. S., Lakshminarayana, S., Vijayan, V., Lakshmi, P. R., Gavarasana, S., and Reddy, S. B. (2006). Trace elemental correlation study in malignant and normal breast tissue by pixe technique. *Nuclear Instruments and Methods in Physics Research Section B: Beam Interactions with Materials and Atoms*, **247**(2), 361–367.

Rizk, S. L. and Sky-Peck, H. H. (1984). Comparison between concentrations of trace elements in normal and neoplastic human breast tissue. *Cancer research*, **44**(11), 5390–5394.

Round, A., Wilkinson, S., Hall, C., Rogers, K., Glatter, O., Wess, T., and Ellis, I. (2005). A preliminary study of breast cancer diagnosis using laboratory based small angle x-ray scattering. *Physics in medicine and biology*, **50**(17), 4159.

Ryan, E. A. and Farquharson, M. J. (2007). Breast tissue classification using x-ray scattering measurements and multivariate data analysis. *Physics in Medicine & Biology*, **52**(22), 6679.

Ryan, E. A., Farquharson, M. J., and Flinton, D. M. (2005). The use of compton scattering to differentiate between classifications of normal and diseased breast tissue. *Physics in medicine and biology*, **50**(14), 3337.

Schrauzer, G. (1980). role of trace elements in the etiology of cancer. In *Trace element analytical chemistry in medicine and biology: proceedings of the first international workshop, Neuherberg, Federal Republic of Germany, April 1980/editors, Peter Bratter, Peter Schramel.* Berlin; New York: De Gruyter, 1980.

Scott, R., Stone, N., Kendall, C., Geraki, K., and Rogers, K. (2016). Relationships between pathology and crystal structure in breast calcifications: an in situ x-ray diffraction study in histological sections. *npj Breast Cancer*, **2**, 16029.

Scott, R., Kendall, C., Stone, N., and Rogers, K. (2017). Elemental vs. phase composition of breast calcifications. *Scientific Reports*, **7**(1), 136.

Siddiqui, M., Singh, S., Mehrotra, P., Singh, K., Sarangi, R., *et al.* (2006). Comparison of some trace elements concentration in blood, tumor free breast and tumor tissues of women with benign and malignant breast lesions: an indian study. *Environment International*, **32**(5), 630–637.

Silva, M., Tomal, A., Perez, C., Ribeiro-Silva, A., and Poletti, M. (2009). Determination of ca, fe, cu and zn and their correlations in breast cancer and normal adjacent tissues. *X-Ray Spectrometry*, **38**(2), 103–111.

Silva, M. P., Soave, D. F., Ribeiro-Silva, A., and Poletti, M. E. (2012a). Trace elements as tumor biomarkers and prognostic factors in breast cancer: a study through energy dispersive x-ray fluorescence. *BMC research notes*, **5**(1), 194.

Silva, M. P. d., Silva, D. M. d., Ribeiro-Silva, A., and Poletti, M. E. (2012b). Correlations of trace elements in breast human tissues: Evaluation of spatial distribution using μ-xrf. In *AIP Conference Proceedings*, volume 1437, pages 45–49. AIP.

Silva, M. P. d., Silva, D., Conceicao, A., Ribeiro-Silva, A., and Poletti, M. (2013). Role of ca, fe, cu and zn in breast cancer: study by x-ray fluorescence techniques and immunohistochemical analysis. *X-Ray Spectrometry*, **42**(4), 303–311.

Silvera, S. A. N. and Rohan, T. E. (2007). Trace elements and cancer risk: a review of the epidemiologic evidence. *Cancer Causes & Control*, **18**(1), 7–27.

Sosa, C., Malezan, A., Poletti, M., and Perez, R. (2017). Compact energy dispersive x-ray microdiffractometer for diagnosis of neoplastic tissues. *Radiation Physics and Chemistry*, **137**, 125–129.

Speller, R. (1999). Tissue analysis using x-ray scattering. *X-Ray Spectrometry*, **28**(4), 224–250.

Tadrous, P. J., Siegel, J., French, P. M., Shousha, S., Lalani, E.-N., and Stamp, G. W. (2003). Fluorescence lifetime imaging of unstained tissues: early results in human breast cancer. *The Journal of pathology*, **199**(3), 309–317.

Thayalan, K. (2014). *The physics of radiology and imaging.* JP Medical Ltd.

Theodorakou, C. and Farquharson, M. J. (2008). Human soft tissue analysis using x-ray or gamma-ray techniques. *Physics in Medicine & Biology*, **53**(11), R111.

Theodorakou, C. and Farquharson, M. J. (2009). The classification of secondary colorectal liver cancer in human biopsy samples using angular dispersive x-ray diffraction and multivariate analysis. *Physics in medicine and biology*, **54**(16), 4945.

Volynskaya, Z., Haka, A. S., Bechtel, K. L., Fitzmaurice, M., Shenk, R., Wang, N., Nazemi, J., Dasari, R. R., and Feld, M. S. (2008). Diagnosing breast cancer using

diffuse reflectance spectroscopy and intrinsic fluorescence spectroscopy. *Journal of biomedical optics*, **13**(2), 024012–024012.

Zhan, X. (2005). Application of polarized edxrf in geochemical sample analysis and comparison with wdxrf. *X-Ray Spectrometry*, **34**(3), 207–212.